



## A singular cell-based smoothed radial point interpolation method for fracture problems

G.R. Liu<sup>a</sup>, Y. Jiang<sup>b,\*</sup>, L. Chen<sup>b</sup>, G.Y. Zhang<sup>c</sup>, Y.W. Zhang<sup>d</sup>

<sup>a</sup> CEAS-Schl Aerospace Systems, Rhodes 733, 2851 Woodside Dr, Cincinnati, OH 45221, USA

<sup>b</sup> Center for Advanced Computations in Engineering Science (ACES), Department of Mechanical Engineering, National University of Singapore, 9 Engineering Drive 1, Singapore 117576, Singapore

<sup>c</sup> Intelligent Systems for Medicine Laboratory, School of Mechanical Engineering, The University of Western Australia, 35 Stirling Highway, Crawley WA6009, Australia

<sup>d</sup> Large-scale Complex Systems, Programme, Institute of High Performance Computing, 1 Fusionopolis Way, Connix, Singapore 138632, Singapore

### ARTICLE INFO

#### Article history:

Received 18 May 2010

Accepted 22 March 2011

Available online 13 April 2011

#### Keywords:

Numerical methods

Meshfree method

Stress intensity factors

Fracture

CS-RPIM

Singularity

### ABSTRACT

A cell-based smoothed radial point interpolation method (CS-RPIM) is developed for fracture problems. The strain smoothing is performed over background triangular cells. The stiffness matrix is calculated based on the weakened weak formulation, using shape functions obtained by radial point interpolation method. A layer of five-node singular elements are used to simulate the singularity around the crack tip. Different schemes are devised in the five-node elements to perform the strain smoothing. Several examples are presented to validate the newly developed method. The results are found in excellent agreement with the exact (or reference) solutions.

© 2011 Elsevier Ltd. All rights reserved.

### 1. Introduction

The stress intensity factor (SIF), which characterizes the stress and displacement distribution around the crack tip, is of great importance and one of the most essential parameters for failure analysis in cracked components. However, analytical solutions for SIFs only exist for some very simple cases, thus numerical methods are usually employed for practical problems that are usually complicated in many ways.

To solve complicated engineering problems, many powerful numerical methods have been proposed, such as finite element methods (FEM) [1–4], finite difference methods [5,6] and finite volume methods (FVM) [7,8]. The FEM is currently the most widely used reliable numerical method in practical application, whereas it has its own shortcomings. The first shortcoming is “overly-stiff” stiffness matrix, which leads to lower bound to the exact solution in the energy norm. The second concerns with mesh distortion-related problems, such as the significant accuracy loss when the element is heavily distorted. In FEM, six-node singular triangular elements are utilized to simulate the singular strain field around the crack tip, while this method needs transitional elements to connect the singular elements to the outer common elements. Recently, the extended finite element method (XFEM) has been

developed for fracture problems [9–12]. However, in the setting of XFEM, a layer of “blending” elements is used in the transition zone from the enrichment to the usual FEM approximation. The usage of the blending elements will produce a local loss of partitions of unity property, which will lead to errors and decrease in convergence rate [13]. Several approaches [14,15] have been proposed to overcome this shortcoming. XFEM has been extended to three-dimensional modeling of crack growth problems [16–20]. Karihaloo and Xiao [21,22] extended the hybrid crack element (HCE) for evaluating the SIF but also the coefficients of the higher order terms of the crack tip asymptotic field. HCE is formulated from a simplified variational functional using truncated asymptotic crack tip displacement. But the exclusion of the rigid body modes in the truncated asymptotic displacements creates jumps between these displacements and element compatible boundary displacements. Also some methods are proposed for this shortcoming.

In recent years, a generalized gradient smoothing technique has been applied and been the foundation of a series of novel and powerful numerical methods [23–27]. A G space theory [28] and weakened weak (W2) formulation [29,30] have been established as a general fundamental theory for meshfree methods [31]. The gradient smoothing technique is also applied to finite element method (FEM) to develop smoothed finite element method (S-FEM [32]) using different kinds of smoothing domains [33]. A node-based smoothed finite element method (NS-FEM) has been developed with the smoothing domains constructed based on nodes of the

\* Corresponding author.

E-mail address: [g0900565@nus.edu.sg](mailto:g0900565@nus.edu.sg) (Y. Jiang).

elements [33]. NS-FEM is found to provide an upper bound solution [33,34]. Moreover, Liu et al. [35,36] formulated an edge-based smoothed finite element method (ES-FEM) which uses smoothing domains constructed based on edges of elements. One of the most obvious advantages of ES-FEM is its super convergence property and high accuracy compared to FEM using the same mesh. With the displacement field obtained by point interpolation method (PIM), a node-based smoothed point interpolation method (NS-PIM) [37–39] has been formulated. The major advantage of PIM is that the shape functions created possess the Kronecker delta function property, which allows simple enforcement of essential boundary conditions as in the conventional FEM. So far, two types of PIM shape functions have been used with different forms of basis functions: polynomial basis functions [40,41] and radial basis functions (RBFs) [42–44]. PIM using radial basis functions (RBFs) is termed as radial PIM (RPIM). Because of the use of local approximation, the stability needs to be ensured via a weak formulation with proper shape parameter control [42–44] or W2 formulation [30]. There are several advantages to use RBF as the basis function in constructing PIM shape functions [41].

1. Using RBF can effectively resolve the singularity problem in the moment matrix of the polynomial PIM [31].
2. RPIM shape functions behave very stably with respect to nodal irregularity and hence are very flexible for arbitrary node distribution.
3. RPIM shape functions can be easily created for three-dimensional domains, because RBF is a function of distance and the only variable is the distance.

Making use of the advantages of RPIM, a cell-based radial point interpolation method (CS-RPIM) is developed for fracture mechanics in this work. In this method, the gradient smoothing procedure is performed over each background triangular cell, with the displacement field approximated using RPIM.

Due to the  $1/\sqrt{r}$  singularity of the strain around the crack tip, properly capturing such singularity is crucial for a numerical method. In order to better capture the singularity in the vicinity of the crack tip, a five-node singular element [34,45] with a  $\sqrt{r}$  displacement field is adopted in our work, shown in Fig. 1. Several smoothing schemes for the singular elements are devised and applied to numerical examples. Intensive examples show that the present singular CS-RPIM improves the accuracy of the solution in terms of SIFs and strain energy in comparison with the standard FEM-T3. Excellent agreement between the numerical results of the present singular CS-RPIM and the corresponding reference solutions is achieved for a wide range of boundary conditions.

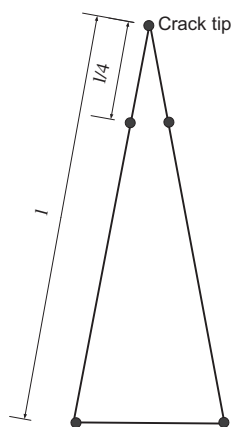


Fig. 1. Five-node element.

## 2. Cell-based radial point interpolation method

### 2.1. Basic equations for 2D solids

Consider a two-dimensional static elasticity problem defined in the domain  $\Omega$  bounded by  $\Gamma$  ( $\Gamma = \Gamma_u + \Gamma_t$ ;  $\Gamma_u \cap \Gamma_t = \emptyset$ ) governed by the following equations. Displacement conditions are prescribed on  $\Gamma_u$ , and tractions are prescribed on  $\Gamma_t$ .

$$\mathbf{L}_d^T \boldsymbol{\sigma} + \mathbf{b} = 0 \quad \text{in } \Omega \quad (1)$$

where  $\mathbf{L}_d$  is a matrix of differential operator defined as:

$$\mathbf{L}_d \left( \frac{\partial}{\partial x}, \frac{\partial}{\partial y} \right) = \begin{bmatrix} \frac{\partial}{\partial x} & 0 \\ 0 & \frac{\partial}{\partial y} \\ \frac{\partial}{\partial y} & \frac{\partial}{\partial x} \end{bmatrix} \quad (2)$$

$\boldsymbol{\sigma}^T = [\sigma_{xx} \ \sigma_{yy} \ \tau_{xy}]$  is the vector that collects stress components and  $\mathbf{b}^T = [b_x \ b_y]$  is the body force vector. The stresses relate the strains via the constitutive equation or the generalized Hooke's law as follows:

$$\boldsymbol{\sigma} = \mathbf{D} \boldsymbol{\varepsilon} \quad (3)$$

in which  $\mathbf{D}$  is the matrix of material constants that is defined in Eq. (4), where  $E$  is Young's modulus and  $\nu$  is Poisson's ratio.

$$\mathbf{D} = \frac{E}{1-\nu^2} \begin{bmatrix} 1 & \nu & 0 \\ \nu & 1 & 0 \\ 0 & 0 & \frac{1-\nu}{2} \end{bmatrix} \quad \text{Plane stress} \quad (4)$$

$$\mathbf{D} = \frac{E(1-\nu)}{(1+\nu)(1-2\nu)} \begin{bmatrix} 1 & \frac{\nu}{1-\nu} & 0 \\ \frac{\nu}{1-\nu} & 1 & 0 \\ 0 & 0 & \frac{1-2\nu}{2(1-\nu)} \end{bmatrix} \quad \text{Plane strain}$$

In Eq. (3),  $\boldsymbol{\varepsilon}^T = [\varepsilon_{xx} \ \varepsilon_{yy} \ 2\varepsilon_{xy}]$  is the vector of strains that is related to the displacements by the following compatibility equation.

$$\boldsymbol{\varepsilon} = \mathbf{L}_d \mathbf{u} \quad (5)$$

where  $\mathbf{u} = [u_x \ u_y]^T$  is the displacement vector. Strains obtained using Eq. (5) are generally called compatible strains.

There are two types of boundary conditions: Dirichlet (or essential/displacement) boundary conditions and Neumann (or natural/stress) boundary conditions.

Dirichlet boundary conditions:

$$\mathbf{u} = \mathbf{u}_r \quad \text{on } \Gamma_u \quad (6)$$

where  $\mathbf{u}_r$  is the vector of the prescribed displacements on the essential boundary  $\Gamma_u$ .

Neumann boundary conditions:

$$\mathbf{L}_n^T \boldsymbol{\sigma} = \mathbf{t}_r \quad \text{on } \Gamma_t \quad (7)$$

where  $\mathbf{t}_r$  is the vector of the prescribed traction on the natural boundary  $\Gamma_t$ , and  $\mathbf{L}_n$  is the matrix of unit outward normal which can be expressed as:

$$\mathbf{L}_n(n_x, n_y) = \begin{bmatrix} n_x & 0 \\ 0 & n_y \\ n_y & n_x \end{bmatrix} \quad (8)$$

### 2.2. Edge based T-schemes of node selection

In this work, all the models are discretized with three-node triangular elements, which also serve as smoothing domains. The points of interest or the quadrature points are located on the edges of background triangular cells. Therefore, nodes need to be selected for the displacement interpolation. Cell-based T-schemes for node

selection have been presented and work well in NS-PIM and ES-PIM models [33,38]. In this work, edge-based T4 scheme is adopted. Edges of the triangles can be classified into two groups: the first is the interior edge, which is located inside the problem domain; the second is the boundary edge, which is located on the model boundaries.

The edge-based T4 scheme selects four nodes for the displacement interpolation of a point located on an interior edge and two nodes for that located on boundary edge. As depicted in Fig. 2, when the point of interest ( $\mathbf{x}$ ) is located on an interior edge, two end nodes and two nodes opposite to the interior edge are selected. These four nodes are numbered for approximating displacement field by the radial point interpolation method. When the point of interest ( $\mathbf{x}$ ) is located on a boundary edge, two end nodes are selected for the displacement interpolation. The displacement along the boundary edge is assumed to be linear interpolation of the two end nodes displacements.

### 2.3. Displacement approximation using RPIM

The displacement field  $u(\mathbf{x})$  along the edge is approximated in a local support domain constructed by a set of selected nodes using radial basis function  $R_i(\mathbf{x})$  augmented with polynomial basis function  $P_j(\mathbf{x})$  [33,46].

$$u(\mathbf{x}) = \sum_{i=1}^n R_i(\mathbf{x})a_i + \sum_{j=1}^m P_j(\mathbf{x})b_j = \mathbf{R}^T(\mathbf{x})\mathbf{a} + \mathbf{P}^T(\mathbf{x})\mathbf{b} \quad (9)$$

where  $n$  is the number of RBFs, which is identical to the number of nodes in the local support domain for the point ( $\mathbf{x}$ ).  $m$  is the number of polynomial basis functions. Coefficients  $a_i$  and  $b_j$  are constants to be determined.

In the radial basis function  $R_i(\mathbf{x})$ , the only variable is the distance between the point of interest ( $x, y$ ) and a node ( $x_i, y_i$ ), where ( $x_i, y_i$ ) is the coordinate of node comprising the support domain. For a 2D problem,  $r$  is defined as:

$$r = [(x - x_i)^2 + (y - y_i)^2]^{1/2} \quad (10)$$

There are four types of radial basis functions (RBFs): multi-quadrics (MQ) function, Gaussian radial function, thin plate spline (TPS) function and Logarithmic radial basis function. In this work, the MQ function with parameters  $\alpha_c$  and  $q$  is adopted to construct RPIM shape functions [41,47].

$$R_i(x, y) = (r_i^2 + (\alpha_c d_c)^2)^q \quad (11)$$

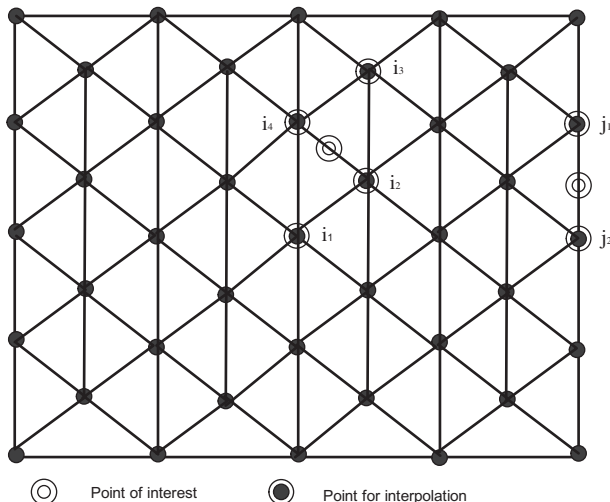


Fig. 2. T4 scheme for node selection for the interpolation at points located at interior side and boundary side.

Here  $\alpha_c = 4.0$ ,  $q = 1.03$  and  $d_c$  is the average dimension of the background triangular cells.  $P_j(\mathbf{x})$  is the basis function of monomials built utilizing the Pascal's triangles.

$$P_j = [1 \ x_1 \ y_1 \ \dots \ p_m(\mathbf{X}_1)] \quad (12)$$

The constants  $a_i$  and  $b_j$  are determined by making Eq. (9) satisfied at these  $n$  nodes in the local support domain. There are  $m + n$  unknowns in Eq. (9), but Eq. (9) consists only  $n$  equations. So another  $m$  equations should be required. Golberg et al. [44] enforced the following  $m$  constraint conditions to be satisfied.

$$\sum_{i=1}^n p_j(x_i)a_i = \mathbf{P}_m^T \mathbf{a} = 0 \quad j = 1, 2, \dots, m \quad (13)$$

Combining Eqs. (9) and (13) yields the following:

$$\tilde{\mathbf{U}}_e = \begin{bmatrix} \mathbf{U}_e \\ \mathbf{0} \end{bmatrix} = \begin{bmatrix} \mathbf{R}_q & \mathbf{P}_m \\ \mathbf{P}_m^T & \mathbf{0} \end{bmatrix} \begin{bmatrix} \mathbf{a} \\ \mathbf{b} \end{bmatrix} = \mathbf{G}\mathbf{a}_0 \quad (14)$$

where

$$\tilde{\mathbf{U}}_e = [u_1 \ u_2 \ \dots \ u_n \ 0 \ 0 \ \dots \ 0]_{(m+n)} \quad (15)$$

$$\mathbf{a}_0^T = [a_1 \ a_2 \ \dots \ a_n \ b_1 \ b_2 \ \dots \ b_m] \quad (16)$$

Then the displacement can be rewritten as:

$$u(\mathbf{x}) = \boldsymbol{\varphi}^T(\mathbf{x})\mathbf{U}_e = \sum_{i=1}^n \phi_i u_i \quad (17)$$

### 2.4. Singular shape function

The most important issue of linear elastic fracture mechanics is that the stress and strain field around the crack tip possesses the singularity of the inverse square root. Common elements can not simulate this kind of stress and strain field. In FEM, singular element is used to deal with the singularity around the crack tip. The most popular singular elements are the eight-node quarter-point element and the six-node quarter-point element. In these elements, the middle nodes of the edges linking to the crack tip are shifted to the quarter points (near the crack tip) of the edges [49,50,9]. However, using this kind of singular element, transitional elements are needed to ensure the compatible displacement field between the singular elements and common elements, which increases the computational cost greatly. In this work, a layer of singular elements [34,45] containing the crack tip are used within the framework of CS-RPIM to construct singular strain field. As shown in Fig. 1, in this singular element an additional node is added to each edge originating from the crack tip. The location of the added node is at one quarter point of the edge from the crack tip. Within this singular element, the displacement is assumed to contain  $\sqrt{r}$  term, thus a  $1/\sqrt{r}$  singular strain and stress field can be created. Within this element, displacement field function  $u(\mathbf{x})$  along the edges originating from the crack tip can be approximated using:

$$u(\mathbf{x}) = a_0 + a_1 r + a_2 \sqrt{r} \quad (18)$$

where  $r$  is the radial distance between the crack tip and the point ( $\mathbf{x}$ ).  $a_0, a_1, a_2$  are the interpolation coefficients corresponding to the given point ( $\mathbf{x}$ ). The coefficients  $a_0, a_1$  and  $a_2$  can be determined by enforcing Eq. (18) to exactly pass through nodal values of the three nodes along the edge.

$$\begin{aligned} u_1 &= a_0 + a_1 r_1 + a_2 \sqrt{r_1} \\ u_2 &= a_0 + a_1 r_2 + a_2 \sqrt{r_2} \\ u_3 &= a_0 + a_1 r_3 + a_2 \sqrt{r_3} \end{aligned} \quad (19)$$

where  $r_1, r_2$  and  $r_3$  are the radial distances between the three nodes and the crack tip, respectively. Solving these three equations for  $a_1, a_2$  and  $a_3$ , and substituting them into Eq. (18) gives us:

$$u(\mathbf{x}) = \left[ \underbrace{1 + 2\frac{r}{l} - 3\sqrt{\frac{r}{l}}}_{\phi_1} \underbrace{- 4\frac{r}{l} + 4\sqrt{\frac{r}{l}}}_{\phi_2} \underbrace{2\frac{r}{l} - \sqrt{\frac{r}{l}}}_{\phi_3} \right] \begin{Bmatrix} u_1 \\ u_2 \\ u_3 \end{Bmatrix} \quad (20)$$

where  $l$  is the length of the edge.  $\phi_1, \phi_2$  and  $\phi_3$  are the shape functions for these three nodes on the edge, respectively.  $u_1, u_2$  and  $u_3$  are the displacements of the three nodes. The displacement along the edge opposite to the crack tip can be constructed by linear interpolation or RPIM to be displacement-compatible with the outside elements. As the strain matrix is calculated by the integration of shape functions multiplied by the component of unit outward vector along the edges of the cell, there will not be singular term in the integrand, which can result in error in the process of Gauss quadrature. This is one of the advantages this singular element shows, compared to other methods. Meanwhile, there are only two nodes along the edge opposite to the crack tip, so the displacement field of this singular element is compatible with common elements. Transitional elements of commonly singular FEM or blending elements of XFEM are not needed in our method.

2.5. Cell-based smoothed strains

The smoothed strains are obtained using the generalized smoothing operation defined in Eq. (21) [29], with displacement fields constructed using RPIM shape functions. The smoothing domains are generally constructed based on the background triangular cells. In the scheme of present CS-RPIM, the triangular background cells serve as smoothing domains. Our shape functions are created for points on the edges of the cells, which are always continuous.

Substituting Eq. (17) into Eq. (21) to perform the strain smoothing operation over each triangular background cell, the cell based smoothed strain  $\bar{\epsilon}_k$  can be given in Eq. (22).

$$\bar{\epsilon}_k(\mathbf{u}) = \frac{1}{A_k^s} \int_{\Gamma_k^s} \mathbf{L}_n \mathbf{u}(\mathbf{x}) ds = [\bar{\epsilon}_{xx} \ \bar{\epsilon}_{yy} \ 2\bar{\epsilon}_{xy}]_k^T \quad (21)$$

$$\bar{\epsilon}_k = \frac{1}{A_k^s} \int_{\Gamma_k^s} \mathbf{L}_n \phi u_i d\Gamma = \sum_{i \in N_{infi}} \bar{\mathbf{B}}_i(x_k) u_i \quad (22)$$

where  $\epsilon$  is the matrix of RPIM shape functions,  $A_k^s$  is the area of the smoothing domain,  $\Gamma_k^s$  is the boundary of the smoothing domain, and  $N_{infi}$  is the number of nodes involved in constructing the displacement fields along the smoothing domain  $\Omega_k^s$ . The smoothed strain matrix  $\bar{\mathbf{B}}_i(\mathbf{x}_k)$  can be expressed as:

$$\bar{\mathbf{B}}_i(x_k) = \begin{bmatrix} \bar{b}_{ix}(x_k) & 0 \\ 0 & \bar{b}_{iy}(x_k) \\ \bar{b}_{iy}(x_k) & \bar{b}_{ix}(x_k) \end{bmatrix} \quad (23)$$

where  $\bar{b}_{ix}(x_k)$  and  $\bar{b}_{iy}(x_k)$  are obtained as:

$$\bar{b}_{il} = \frac{1}{A_k^s} \int_{\Gamma_k^s} \phi_i(x_k) n_l(x_k) d\Gamma \quad (24)$$

Note that the above integrand does not contain any singular term so that it can be performed using the standard Gauss quadrature. By Gauss quadrature, the above equation can be expressed as:

$$\bar{b}_{il} = \frac{1}{A_k^s} \sum_{m=1}^{N_{seg}} \left[ \sum_{n=1}^{N_{gau}} w_n \phi_i(x_k) n_l(x_k) \right] \quad (l = x, y) \quad (25)$$

where  $N_{seg}$  is the number of segments the boundary  $\Gamma_k^s$  consists of ( $N_{seg} = 3$ ).  $N_{gau}$  is the number of Gauss points used on each segment and  $w_n$  is the corresponding weight of Gauss quadrature point.

Based on the CS-RPIM procedure, the entry of the global stiffness matrix of the whole model is a summation of the sub-matrixes of the stiffness matrix associated with all the cell-based smoothing domains.

$$\bar{\mathbf{K}}_{ij} = \sum_{k=1}^{N_s} \bar{\mathbf{K}}_{ij,k} \quad (26)$$

where  $\bar{\mathbf{K}}_{ij}$  is the  $ij$ th entry of the global stiffness matrix and  $\bar{\mathbf{K}}_{ij,k}$  is that of the stiffness matrix of the  $k$ th smoothing domain, and  $N_s$  is the total number of smoothing domains. Because the strains within the smoothing domain is assumed to be constant,  $\bar{\mathbf{K}}_{ij,k}$  can be obtained simply by Eq. (27), without integration.

$$\bar{\mathbf{K}}_{ij,k} = \mathbf{A}_k^s \bar{\mathbf{B}}_i^T \mathbf{D} \bar{\mathbf{B}}_j \quad (27)$$

We note here again that there is no need for numerical integration for computing the stiffness matrix (unlike the standard weak formulations). All we need is the simple and standard (no-singular) integration performed in Eqs. (24) and (25).

2.6. Different schemes of strain smoothing in the singular element

In order to capture the singularity of the stress and strain field around the crack tip more accurately, several smoothing schemes have been adopted over the five-node singular elements around the crack tip.

2.6.1. SCS-RPIM-2d

In this scheme, the two quarter nodes are linked with a line, which divides the five-node element into two smoothing domains (ADE and BCDE) shown in Fig. 3(a). In the singular element, the displacement fields along edges AB and AC are approximated by Eq. (20). The displacement along edge DE is assumed to be linear interpolation of  $u_D$  and  $u_E$ . In order to have a compatible displacement field with the connected common triangular element, which shares the same edge BC with the singular element, the displacement field along BC is approximated by cell-based radial point interpolation method. The support domain is selected by T4 node selection scheme just taking nodes A, B and C into consideration, neglecting nodes D and E. Two smoothing domains comprise the singular element. The strain smoothing operation is performed over ADE and BCDE respectively. This scheme is named as SCS-RPIM-2d to be referred to in our later discussion.

2.6.2. SCS-RPIM-4d

In order to have the effect of finer mesh around the crack tip, the singular element is split into four domains in this scheme. Four more points are added to the middle points of edges AD, DB, AE and EC, respectively, without increasing the number of DOFs (degrees of freedom) in the whole model. These four points will partition the element into four smoothing domains (AFG, FGDE, DHIE and HIBC) by linking DE, FG and HI, shown in Fig. 3(b). The displacements of these four points can be interpolated by the displacement of the three nodes on the same edges using Eq. (20). In the singular element, we approximate displacement fields along FG, DE and HI by linear interpolation of their own two-end nodes (or points) displacements, respectively. The displacement field along edge BC is in the same manner as mentioned in scheme SCS-RPIM-2d. The smoothing operations are performed over four domains independently. Due to the four smoothing domains associated with each singular element around the crack tip, this scheme is thus named SCS-RPIM-4d.

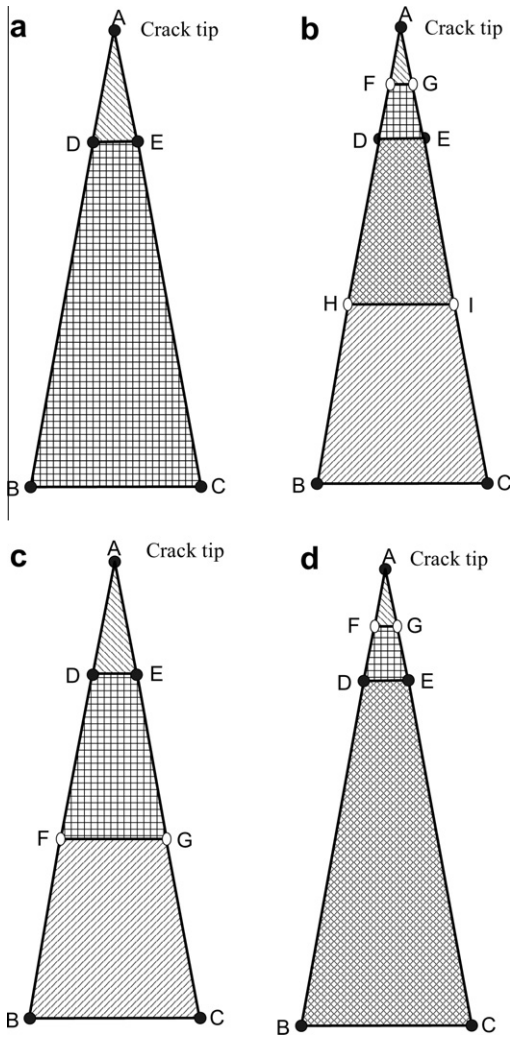


Fig. 3. Different schemes of strain smoothing (a) SCS-RPIM-2d, (b) SCS-RPIM-4d, (c) SCS-RPIM-3d, (d) SCS-RPIM-3d2 (different types of shadows stand for different smoothing domains).

2.6.3. SCS-RPIM-3d

In this scheme, two additional points (F, G) are employed to divide the singular element into three smoothing domains (ADE, DFGE and FBCG) by linking DE and FG shown in Fig. 3(c). The smoothing operation can be performed over each of the three domains. This scheme is named as SCS-RPIM-3d. The two points are arranged to the middle points of DB and EC, without increasing the number of DOFs. The displacement fields along DE and FG can be obtained by linear interpolation of the two end nodes (or points) displacements. The displacement field along BC is obtained in the same way as mentioned in SCS-RPIM-2d.

2.6.4. SCS-RPIM-3d2

The only difference between this scheme and previous SCS-RPIM-3d is the locations of the two newly added points (F, G), which are shifted to the middle points of DB and EC in this scheme. All other settings are the same with SCS-RPIM-3d. The three domains ADE, DFGE and FBCG are shown in Fig. 3(d). In order to be different from SCS-RPIM-3d, this scheme is termed as SCS-RPIM-3d2.

2.6.5. ST5-T3

In order to better validate the way of dealing with singularity in this paper, ST5-T3 scheme is devised in this paper. In this scheme, a

layer of five-node elements are adopted around the crack tip, and the singular element is divided into two smoothing domains, with smoothing operation performed over each of the two domains. All the other elements are 3-node triangular elements. The displacement field in other elements is in the same manner as that of FEM-T3. The stiffness matrix is obtained in the same way as what we do in FEM. Note that in order to have a compatible displacement field with the connected triangular element, which shares the same edge BC, the displacement field along edge BC is produced by linear interpolation of  $u_B$  and  $u_C$ . Therefore this scheme is named as ST5-T3.

3. Domain interaction integral methods for 2D fracture problems

The interaction integral method [9,10] is one of the methods to calculate stress intensity factor in fracture mechanics. In this method, there are two states of a cracked body considered. One is the present state to be solved with the parameters of  $(\sigma_{ij}^{(1)}, \epsilon_{ij}^{(1)}, u_i^{(1)})$ , and the other is an auxiliary state with the parameters of  $(\sigma_{ij}^{(2)}, \epsilon_{ij}^{(2)}, u_i^{(2)})$ , which could be a state of pure mode I or pure mode II. Two simple conditions exist for the stress intensity factors regarding the auxiliary fields.

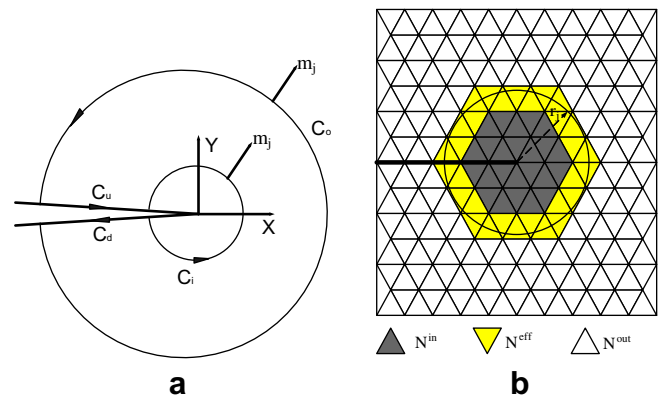


Fig. 4. (a) Integration domain is enclosed by  $C = C_o + C_i + C_u + C_d$ ,  $n_j = m_j$  on  $C_o, C_u, C_d$ ,  $n_j = -m_j$  on  $C_i$  (b) different types of elements around the crack tip for the area integration.

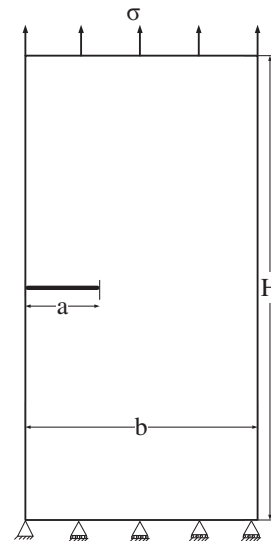


Fig. 5. Plate with edge crack under remote tension.

$$\begin{aligned}
 K_I^{(2)} &= 1 \text{ and } K_{II}^{(2)} = 0, \quad \text{for pure mode I} \\
 K_I^{(2)} &= 0 \text{ and } K_{II}^{(2)} = 1, \quad \text{for pure mode II}
 \end{aligned}
 \tag{28}$$

In fracture mechanics, the general form of  $J$ -contour integral can be expressed as follows:

$$J = \int_{\Gamma} \left( \frac{1}{2} \sigma_{ik} \varepsilon_{ik} \delta_{xj} - \sigma_{ij} u_{i,x} \right) n_j d\Gamma
 \tag{29}$$

Also the superimposition can be applied to linear elastic fracture mechanics. Hence, we have:

$$\begin{aligned}
 K_I^{(1+2)} &= K_I^{(1)} + K_I^{(2)} \\
 K_{II}^{(1+2)} &= K_{II}^{(1)} + K_{II}^{(2)}
 \end{aligned}
 \tag{30}$$

Then the value of  $J$ -contour integral for the mixed state of 1 and 2 can be derived.

$$\begin{aligned}
 J^{(1+2)} &= \int_{\Gamma} \left( \frac{1}{2} (\sigma_{ij}^{(1)} + \sigma_{ij}^{(2)}) (\varepsilon_{ij}^{(1)} + \varepsilon_{ij}^{(2)}) \delta_{ij} \right. \\
 &\quad \left. - (\sigma_{ij}^{(1)} + \sigma_{ij}^{(2)}) \frac{\partial (u_i^{(1)} + u_i^{(2)})}{\partial x_1} \right) n_j d\Gamma
 \end{aligned}
 \tag{31}$$

Expanding and rearranging Eq. (31) yields:

$$J^{(1+2)} = J^{(1)} + J^{(2)} + I^{(1,2)}
 \tag{32}$$

where  $I^{(1,2)}$  is named the interaction integral for states 1 and 2, and can be expressed as:

$$I^{(1,2)} = \int_{\Gamma} \left( \sigma_{ik}^{(1)} \varepsilon_{ik}^{(2)} \delta_{xj} - \sigma_{ij}^{(1)} u_{i,x}^{(2)} - \sigma_{ij}^{(2)} u_{i,x}^{(1)} \right) n_j d\Gamma
 \tag{33}$$

$J^{(1+2)}$  can also be given by Eq. (34):

$$J^{(1+2)} = \frac{(K_I^{(1+2)})^2}{E^*} + \frac{(K_{II}^{(1+2)})^2}{E^*}
 \tag{34}$$

Substituting Eq. (30) into Eq. (34) gives us:

$$J^{(1+2)} = J^{(1)} + J^{(2)} + \frac{2}{E^*} (K_I^1 K_I^2 + K_{II}^1 K_{II}^2)
 \tag{35}$$

Comparing Eqs. (32) and (35), we can arrive at

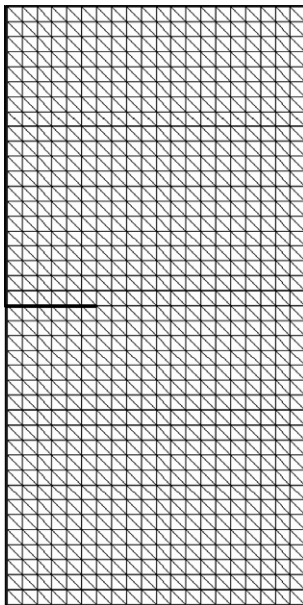


Fig. 6. Mesh of plate with edge crack (21nodes × 41nodes).

Table 1  
The effect of the number of Gauss points on the strain energy and  $K_I$ .

$N_{gau}$	Strain energy ( $\times 10^{-3}$ )	$K_I$
1	1.14196283	1.593119
2	1.15993944	1.646992
3	1.15983803	1.646683
4	1.15983861	1.646683
5	1.15983867	1.646683
6	1.15983867	1.646683
7	1.15983867	1.646683

Table 2  
The variation of  $K_I$  with the integration domain radius.

Mesh/ $r_c$	$31 \times 61$	$41 \times 81$	$51 \times 101$	$61 \times 121$	$71 \times 141$	$81 \times 161$
2.0	1.5982	1.6051	1.6079	1.6093	1.6102	1.6107
2.5	1.5984	1.6050	1.6077	1.6090	1.6098	1.6103
3.0	1.5985	1.6051	1.6079	1.6093	1.6100	1.6105
3.5	1.5985	1.6051	1.6079	1.6093	1.6101	1.6106
4.0	1.5986	1.6052	1.6080	1.6093	1.6101	1.6106
4.5	1.5986	1.6051	1.6078	1.6092	1.6100	1.6105

$$I^{(1,2)} = \frac{2}{E^*} (K_I^1 K_I^2 + K_{II}^1 K_{II}^2)
 \tag{36}$$

Substituting Eq. (28) into Eq. (36) yields:

$$\begin{aligned}
 K_I^{(1)} &= \frac{E^*}{2} I^{(1, \text{Mode I})} \\
 K_{II}^{(1)} &= \frac{E^*}{2} I^{(1, \text{Mode II})}
 \end{aligned}
 \tag{37}$$

In order to get stress intensity factor, the integral in Eq. (33) should be obtained. According to the Divergence theorem, the path integral can be transformed into area integral by multiplying the integrand of Eq. (33) by a weighting function  $q$ .  $q$  is set to be 1 inside the area enclosed by the integral path and 0 outside the area. Then Eq. (33) can be rewritten as:

$$I^{(1,2)} = \int_C \left( \sigma_{ik}^{(1)} \varepsilon_{ik}^{(2)} \delta_{xj} - \sigma_{ij}^{(1)} u_{i,x}^{(2)} - \sigma_{ij}^{(2)} u_{i,x}^{(1)} \right) n_j q d\Gamma
 \tag{38}$$

where  $C = C_o + C_i + C_u + C_d$  and  $n_j$  is the unit outward vector of  $C$ , where  $n_j = m_j$  on  $C_o$ ,  $C_u$  and  $C_d$ ,  $n_j = -m_j$  on  $C_i$ , shown in Fig. 4.

Using the Divergence theorem and passing to the limit as the contour  $C_i$  is shrunk to the crack tip, gives the following equation for the area–path interaction integral in domain form:

$$I^{(1,2)} = - \int_A \left( \sigma_{ik}^{(1)} \varepsilon_{ik}^{(2)} \delta_{xj} - \sigma_{ij}^{(1)} u_{i,x}^{(2)} - \sigma_{ij}^{(2)} u_{i,x}^{(1)} \right) \frac{\partial q}{\partial x_j} dA
 \tag{39}$$

For the above integral, shown in Fig. 4, the domain  $A$  is set to be the collection of all the elements that have a node within a radius of  $r_j = r_c \times d$  ( $r_c$  is a dimensionless parameter,  $d$  is the average dimension of the singular elements around the crack tip) and this element set is denoted as  $N$ .

The weighting function  $q$  is defined as mentioned above. So the gradient of  $q$  within the element belonging to  $N^{in}$  (the nodes of which are all inside  $A$ ), has no contribution to the interaction integral, and non-zero contribution to the integral is obtained only for elements set  $N^{eff}$  with an edge that intersects the boundary of  $A$ . Therefore, Eq. (39) can be rewritten as:

$$I^{(1,2)} = - \sum_{n=1}^{N^{eff}} \int_{A_{eff,n}} \left( \sigma_{ik}^{(1)} \varepsilon_{ik}^{(2)} \delta_{xj} - \sigma_{ij}^{(1)} u_{i,x}^{(2)} - \sigma_{ij}^{(2)} u_{i,x}^{(1)} \right) \frac{\partial q}{\partial x_j} dA
 \tag{40}$$

where  $A_{eff,n}$  is domain of the  $n$ th element in the elements set  $N^{eff}$ .

**Table 3**  
Strain energy ( $\times 10^{-3}$ ) using CS-RPIM of plate with edge crack under remote tension with mesh ( $21 \times 41$ ) of different irregularities.

$r$	0	0.005	0.01	0.02	0.03	0.04	0.05
Strain energy	1.136669	1.136707	1.136780	1.136940	1.136517	1.136269	1.138268

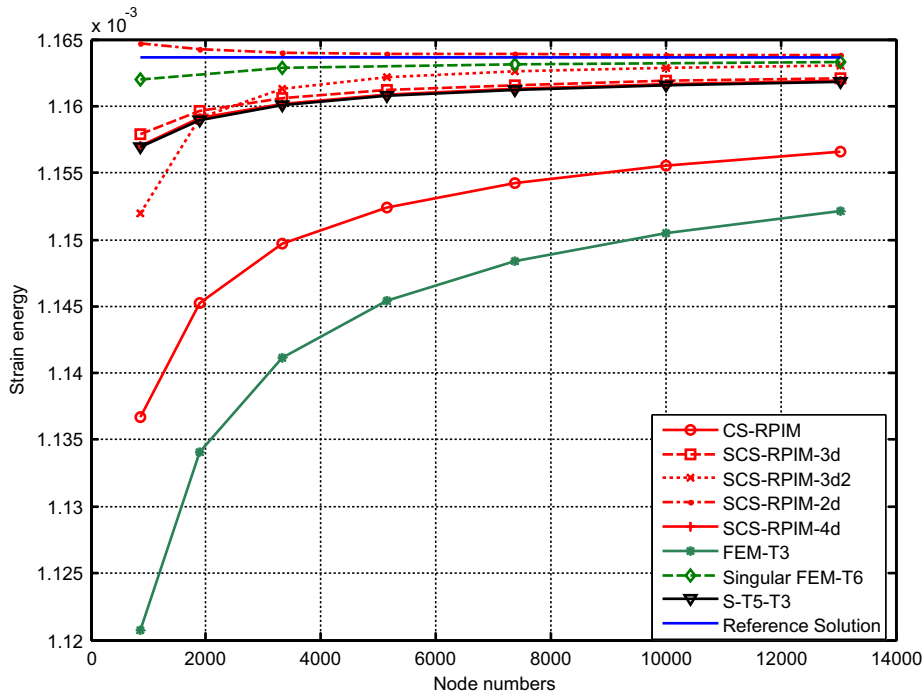


**Fig. 7.** Plate with edge crack under tension: the variation of strain energy with different node numbers by different methods.

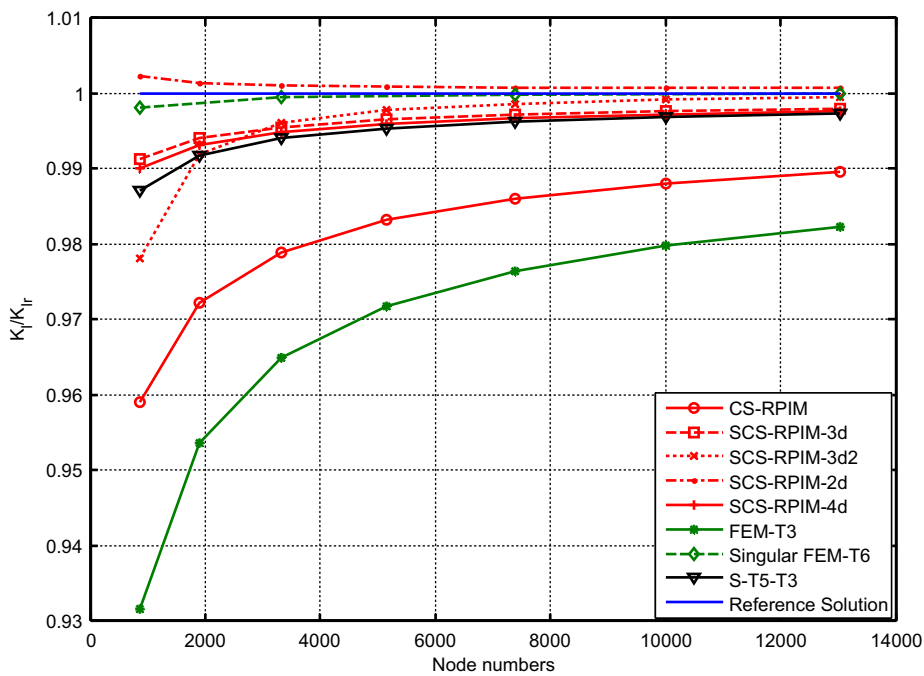


**Fig. 8.** Plate with edge crack under tension: the variation of normalized  $K_I$  with different node numbers by different methods.

**Table 4**Plate with edge crack under remote tension: strain energy with different meshes and different schemes ( $\times 10^{-3}$ ) (reference solution is  $1.1637 \times 10^{-3}$ ).

Mesh	$21 \times 41$	$31 \times 61$	$41 \times 81$	$51 \times 101$	$61 \times 121$	$71 \times 141$	$81 \times 161$
CS-RPIM	1.1367	1.1453	1.1497	1.1524	1.1543	1.1556	1.1566
SCS-RPIM-3d	1.1579	1.1597	1.1606	1.1612	1.1616	1.1619	1.1621
SCS-RPIM-3d2	1.1520	1.1591	1.1613	1.1622	1.1626	1.1629	1.1630
SCS-RPIM-2d	1.1647	1.1642	1.1640	1.1639	1.1639	1.1638	1.1638
SCS-RPIM-4d	1.1570	1.1591	1.1602	1.1608	1.1613	1.1616	1.1619
FEM-T3	1.1207	1.1341	1.1411	1.1455	1.1484	1.1505	1.1521
Singular FEM-T6	1.1620		1.1629		1.1631		1.1633
ST5-T3	1.1569	1.1589	1.1601	1.1607	1.1612	1.1615	1.1618

**Table 5**Plate with edge crack under remote tension: normalized  $K_I$  with different meshes and different schemes (reference solution is 1).

Mesh	$21 \times 41$	$31 \times 61$	$41 \times 81$	$51 \times 101$	$61 \times 121$	$71 \times 141$	$81 \times 161$
CS-RPIM	0.9591	0.9722	0.9790	0.9832	0.9861	0.9881	0.9897
SCS-RPIM-3d	0.9913	0.9941	0.9956	0.9965	0.9972	0.9977	0.9980
SCS-RPIM-3d2	0.9782	0.9920	0.9960	0.9978	0.9987	0.9991	0.9995
SCS-RPIM-2d	1.0023	1.0013	1.0011	1.0009	1.0008	1.0008	1.0007
SCS-RPIM-4d	0.9901	0.9931	0.9949	0.9960	0.9967	0.9972	0.9977
FEM-T3	0.9316	0.9536	0.9649	0.9718	0.9764	0.9798	0.9823
Singular FEM-T6	0.9981		0.9994		0.9998		1.0001
ST5-T3	0.9871	0.9918	0.9941	0.9954	0.9962	0.9968	0.9973

#### 4. Numerical implementation

The numerical implementation procedure of the singular CS-RPIM is listed as follows:

- (1) Mesh the domain; obtain node coordinate and element information.
- (2) Find the support domain for edges of common elements according to edge based T-schemes of node selection, and edges originating from the crack tip using the schemes listed in Section 2.6.
- (3) Loop over cells.
  - (I) Obtain the outward unit normal vector of the edge.
  - (II) Calculate the smoothed strain gradient matrix  $\bar{\mathbf{B}}$  by using Eqs. (23)–(25) for normal cells and crack tip element cells according to different schemes, respectively.
- (III) Substitute  $\bar{\mathbf{B}}$  into Eq. (27) to give the stiffness matrix  $I_j$ th entry.
- (IV) Assemble the global stiffness matrix of the problem.
- (4) Implement boundary conditions including the displacement boundary conditions and stress boundary conditions.
- (5) Solve the equation and obtain the displacements of nodes.
- (6) Calculate the parameters needed, such as strain energy, strain, stress and stress intensity factors.

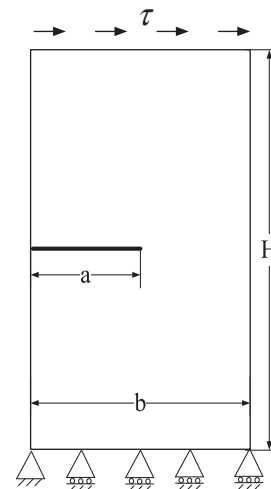
#### 5. Numerical examples

Three examples are presented in this work to testify our methods, rectangular plate with a single edge crack under tension, rectangular plate with a single edge crack under shear and an inclined

**Table 6**

The comparison of strain energy and error for plate with edge crack under remote tension by between SCS-RPIM-2d and singular FEM-T6.

Node number	SCS-RPIM-2d (error %)	Singular FEM-T6 (error %)
861	0.001164677 (0.086)	0.001162022 (0.142)
3321	0.001164039 (0.0317)	0.001162867 (0.069)
7381	0.001163881 (0.0182)	0.00116314 (0.0455)
13,041	0.001163814 (0.0124)	0.001163274 (0.0340)

**Fig. 9.** Plate with edge crack under shear.

crack in rectangular plate under tension. Different schemes are used in our calculation. Strain energy and stress intensity factors (SIFs) of different schemes are calculated and compared.

##### 5.1. Rectangular plate with an edge crack under tension

An edge crack in a plate under tension is first analyzed shown in Fig. 5. The dimensions of the model are: the width  $b = 1$  mm, the height  $H = 2$  mm and the crack length  $a = 0.3$  mm. The load  $\sigma = 1$  Pa is loaded on the top edge of the plate. The material parameters are: Young's modulus  $E = 1 \times 10^3$  MPa and the Poisson's ratio  $\nu = 0.3$ . The displacements in the  $y$  direction are fixed at the bottom edge and the plate is clamped at the bottom left corner. Assume the plate is under plane strain.

##### 5.1.1. Influence of the number of gauss points

Gauss quadrature method is used in the process of numerical integration along each edge of smoothing domains, see Eq. (25). The number of Gauss points affects both the accuracy of the re-

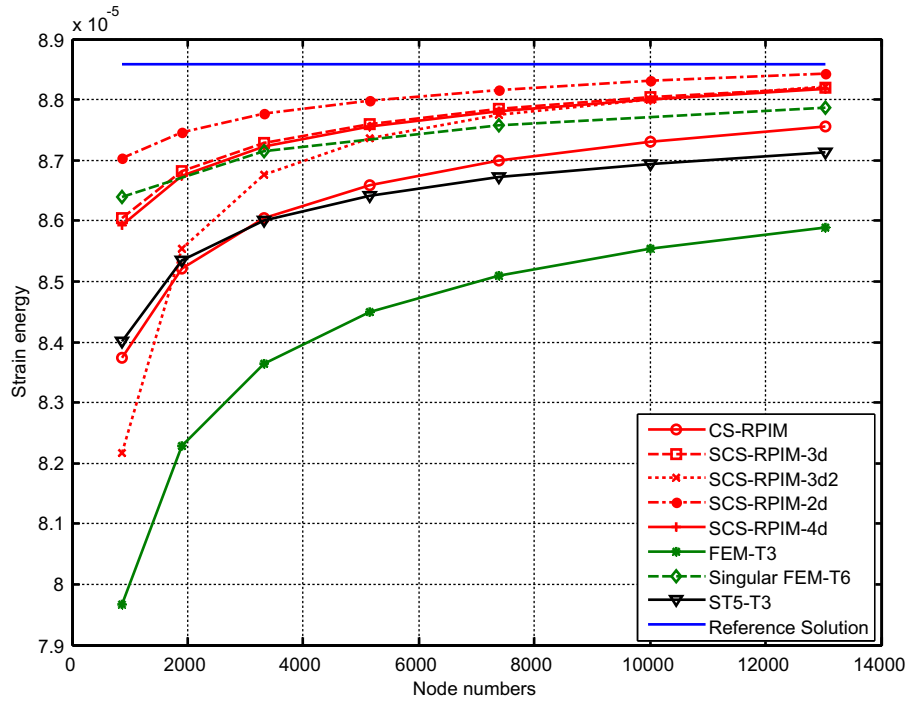


Fig. 10. Plate with edge crack under shear: the variation of normalized strain energy with different node numbers by different methods.

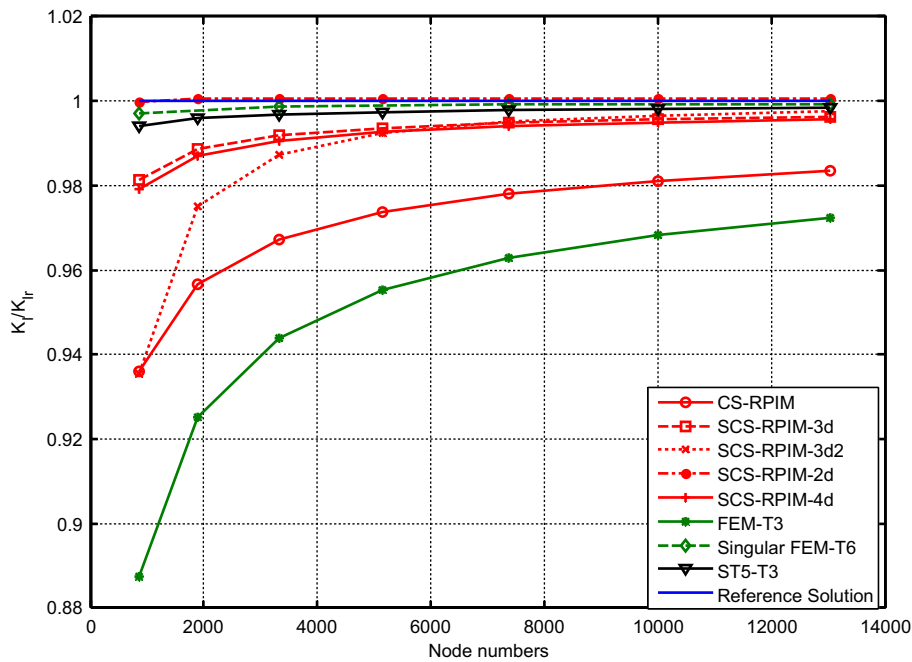


Fig. 11. Plate with edge crack under shear: the variation of normalized  $K_I$  with different node numbers by different methods.

sults and the computational cost in our calculation. Thus using the computed strain energy and SIFs as index parameters, we first study the influence of the Gauss point number on the numerical results. In this study, the SCS-RPIM-4d scheme is used with a mesh of  $21 \times 41$  shown in Fig. 6. The results are listed in Table 1. From the results, it can be seen that the strain energy and the SIFs stay nearly constant when more than three Gauss points are used. So in our later calculation, four Gauss points are used in the numerical integration along each edge of the smoothing domain.

### 5.1.2. Domain independence study

In linear elastic fracture mechanics, the SIFs should be domain independent. In order to check the validity of our methods, the influence of the integration domain on the SIFs is studied. The SCS-RPIM-3d2 is used with several integration domain sizes and different meshes, and the computed SIFs are listed in Table 2. As can be seen, with different mesh densities, when  $r_c$  is greater or equal to 3.0, the SIFs remain nearly the same for different  $r_c$ . So in this work,  $r_c = 3.0$  is used to determine the dimension of the interaction integral domain for all computations.

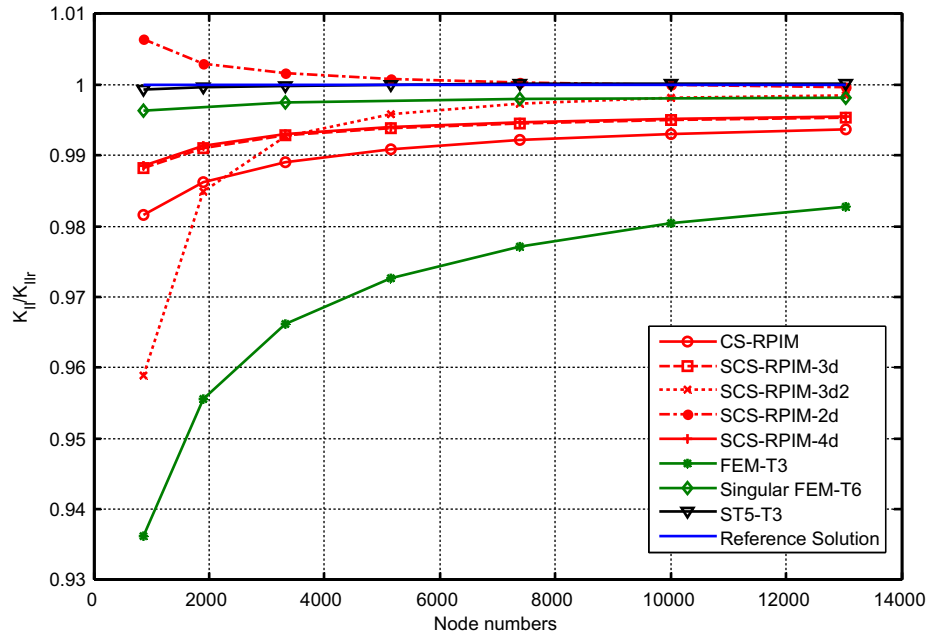


Fig. 12. Plate with edge crack under shear: the variation of normalized  $K_{II}$  with different node numbers by different methods.

Table 7

Plate with edge crack under shear: strain energy with different meshes and different schemes ( $\times 10^{-5}$ ) (reference solution is  $8.8879 \times 10^{-5}$ ).

Mesh	$21 \times 41$	$31 \times 61$	$41 \times 81$	$51 \times 101$	$61 \times 121$	$71 \times 141$	$81 \times 161$
CS_RPIM	8.3748	8.5214	8.6042	8.6593	8.6995	8.7306	8.7557
SCsRPIM_3d	8.6039	8.6821	8.7280	8.7599	8.7842	8.8038	8.8201
SCS_RPIM_3d2	8.2165	8.5548	8.6758	8.7369	8.7745	8.8009	8.8210
SCS_RPIM_2d	8.7028	8.7468	8.7760	8.7981	8.8159	8.8308	8.8437
SCS_RPIM_4d	8.5929	8.6747	8.7225	8.7555	8.7805	8.8006	8.8173
FEM-T3	7.9678	8.2278	8.3638	8.4494	8.5093	8.5542	8.5894
Singular FEM-T6	8.6391		8.7153		8.7571		8.7864
ST5-T3	8.4018	8.5348	8.6008	8.6422	8.6717	8.6945	8.7129

Table 8

Plate with edge crack under shear: normalized  $K_I$  with different meshes and different schemes (reference solution is 1).

Mesh	$21 \times 41$	$31 \times 61$	$41 \times 81$	$51 \times 101$	$61 \times 121$	$71 \times 141$	$81 \times 161$
CS-RPIM	0.9360	0.9567	0.9673	0.9737	0.9781	0.9812	0.9835
SCs-RPIM-3d	0.9814	0.9885	0.9918	0.9936	0.9948	0.9956	0.9962
SCS-RPIM-3d2	0.9355	0.9752	0.9874	0.9925	0.9951	0.9966	0.9975
SCS-RPIM-2d	0.9997	1.0005	1.0007	1.0007	1.0007	1.0007	1.0006
SCS-RPIM-4d	0.9793	0.9871	0.9907	0.9927	0.9941	0.9950	0.9957
FEM-T3	0.8874	0.9251	0.9440	0.9553	0.9629	0.9682	0.9723
Singular FEM-T6	0.9972		0.9987		0.9991		0.9994
ST5-T3	0.9942	0.9960	0.9969	0.9975	0.9979	0.9982	0.9984

Table 9

Plate with edge crack under shear: normalized  $K_{II}$  with different meshes and different schemes (reference solution is 1).

Mesh	$21 \times 41$	$31 \times 61$	$41 \times 81$	$51 \times 101$	$61 \times 121$	$71 \times 141$	$81 \times 161$
CS-RPIM	0.9815	0.9862	0.9891	0.9909	0.9921	0.9930	0.9937
SCs-RPIM-3d	0.9883	0.9911	0.9928	0.9938	0.9945	0.9950	0.9953
SCS-RPIM-3d2	0.9590	0.9849	0.9928	0.9959	0.9974	0.9981	0.9985
SCS-RPIM-2d	1.0064	1.0030	1.0016	1.0009	1.0004	1.0000	1.0000
SCS-RPIM-4d	0.9886	0.9913	0.9930	0.9942	0.9947	0.9951	0.9955
FEM-T3	0.9363	0.9556	0.9661	0.9727	0.9772	0.9804	0.9828
Singular FEM-T6	0.9964		0.9974		0.9979		0.9982
ST5-T3	0.9993	0.9997	0.9998	1.0001	1	1.0002	1.0002

5.1.3. The sensitivity of RPIM to the nodes distribution

All the methods devised in this work are based on RPIM. RPIM is reported to be effective for arbitrarily distributed nodes. However,

for fracture mechanics it is not clear whether RPIM is sensitive to nodes distribution. So it is necessary to investigate the influence of irregularity of the nodes distribution on the results of RPIM.

**Table 10**  
The comparison of strain energy ( $\times 10^{-5}$ ) and error for plate with edge crack under remote tension by between SCS-RPIM-2d and singular FEM-T6.

Node number	SCS-RPIM-2d (error %)	Singular FEM-T6(error %)
861	8.702759 (2.08)	8.639063 (2.80)
3321	8.775995 (1.26)	8.715257 (1.94)
7381	8.815871 (0.811)	8.757142 (1.47)
13,041	8.843731 (0.497)	8.786392 (1.14)

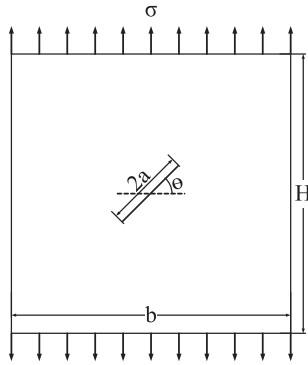


**Fig. 13.** An inclined crack in rectangular plate under tension.

In order to investigate the influence of nodes distribution, we introduce a parameter  $r$  to cause irregularity in the meshes in Fig. 6. A number  $c$  is randomly produced from (0, 1).

$$\begin{aligned} X_{ir} &= X_r + h_x r(2c - 1) \\ Y_{ir} &= Y_r + h_y r(2c - 1) \end{aligned} \tag{41}$$

Here  $(X_r, Y_r)$  are the nodes coordinate of regular mesh  $(X_{ir}, Y_{ir})$  are the nodes coordinate of irregular mesh.  $h_x$  is the average distance of two adjacent nodes in X direction and  $h_y$  is the average distance of two adjacent nodes in Y direction. Different values of  $r$  are used to introduce different degrees of irregularity. The strain energy of the first example with  $21 \times 41$  nodes meshes against the irregularity

parameter  $r$  is listed in Table 3. From Table 3, it can be seen that the strain energy doesn't demonstrate much fluctuation with the change of  $r$ . The largest difference of the strain energy between the irregular mesh and the regular mesh is 0.14%, which is insignificant. Consequently the influence of irregularity on the results of CS-RPIM can be neglected.

**5.1.4. The results**

In this work different mesh densities ( $21 \times 41, 31 \times 61, 41 \times 81, 51 \times 101, 61 \times 121, 71 \times 141$  and  $81 \times 161$ ) are used to discretize the model, as shown in Fig. 6. For the purpose of comparison, numerical results obtained using the FEM-T3 and the singular FEM-T6 are also provided, as well as the methods presented in this work.

The reference solution for strain energy is calculated using the singular FEM-T6 with a very fine mesh (340,630 nodes). The exact solution of SIF is obtained by Eq. (42).

$$K_{Ir} = C\sigma\sqrt{\pi a} \tag{42}$$

where  $C$  is given in Eq. (43):

$$\begin{aligned} C &= 1.12 - 0.231\left(\frac{a}{b}\right) + 10.55\left(\frac{a}{b}\right)^2 - 21.72\left(\frac{a}{b}\right)^3 \\ &\quad + 30.39\left(\frac{a}{b}\right)^4 \end{aligned} \tag{43}$$

Here  $a$  and  $b$  are the crack length and the width of the plate, respectively.

SIFs are normalized by the exact solutions given in Eq. (42). The strain energy and the normalized SIFs obtained using different methods with different mesh densities are plotted in Figs. 7 and 8, and the detailed values are listed in Tables 4 and 5. It can be seen that the strain energy and the SIFs of the CS-RPIM and different schemes of singular CS-RPIM are closer to the reference solution or exact solution than those of FEM-T3 with the same DOFs. Among the different schemes proposed in this work, SCS-RPIM-2d provides an upper bound solution for both strain energy and SIFs with excellent accuracy and other schemes also provide more accurate solution than FEM-T3. This can be an evidence of the high

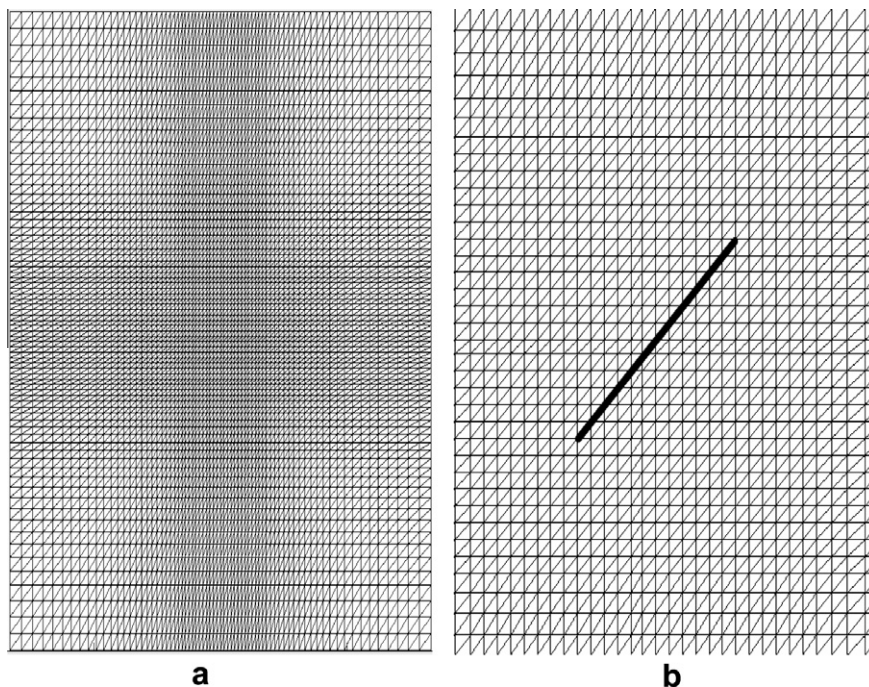


**Fig. 14.** Plate with an inclined crack: (a) mesh of the whole model (73nodes  $\times$  73nodes) and (b) mesh around of the crack.

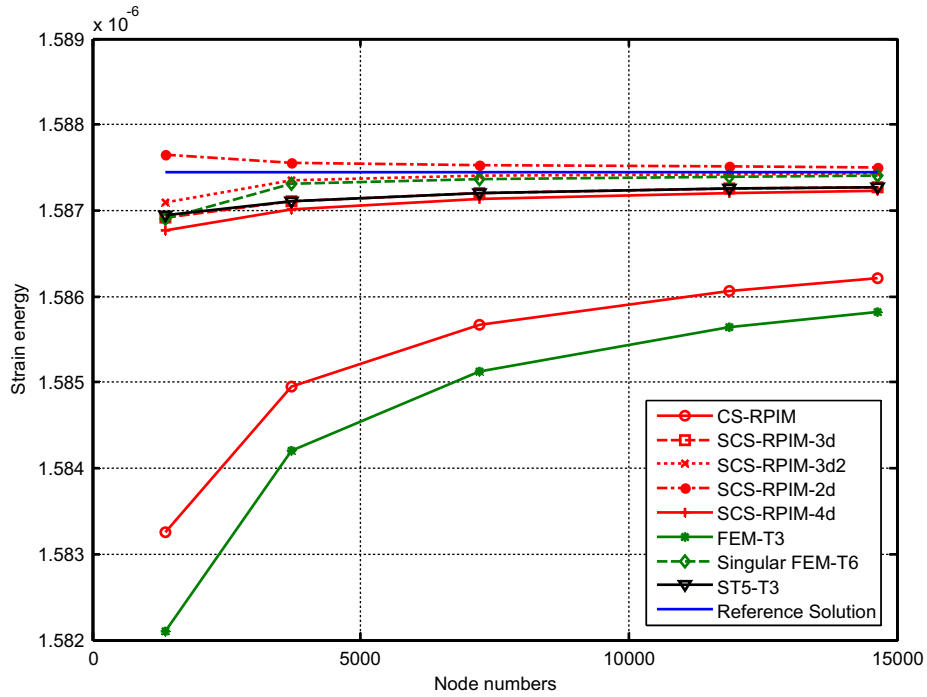


Fig. 15. An 45° inclined crack in rectangular plate under tension: the variation of strain energy with different node numbers by different methods.

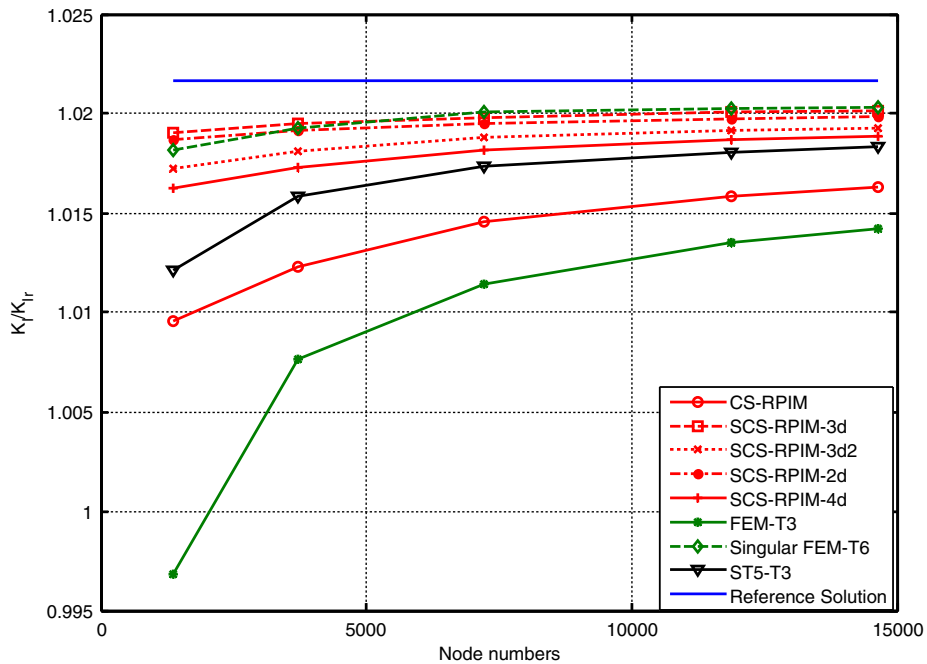


Fig. 16. An 45° inclined crack in rectangular plate under tension: the variation of normalized  $K_I$  with different node numbers by different methods.

efficiency of the singular element around the crack tip adopted in this paper. The strain energy errors of SCS-RPIM-2d and singular FEM-T6 compared to the reference solution are listed in Table 6. From the comparison, it can be seen that the results of SCS-RPIM-2d are closer to the reference solution than singular FEM-T6.

### 5.2. Rectangular plate with an edge crack under shear

In the previous example, we only considered pure Mode I case, for which our method can have more accurate results than FEM-

T3. Now we consider an edge cracked rectangular plate under remote shear tractions, which is a mixed-mode case containing both mode I and II. The dimension of the plate is 16 mm × 7 mm, the crack length  $a = 3.5$  mm and boundary conditions are shown in Fig. 9. The Young's modulus  $E = 3 \times 10^7$  Pa and Poisson's ratio  $\nu = 0.25$  are used in this case. The load  $\tau = 1.0$  Pa is applied on the top edge of the model. The model is under plane strain condition. The mesh densities adopted in this example are the same as the previous example. Also different methods are applied to this example.

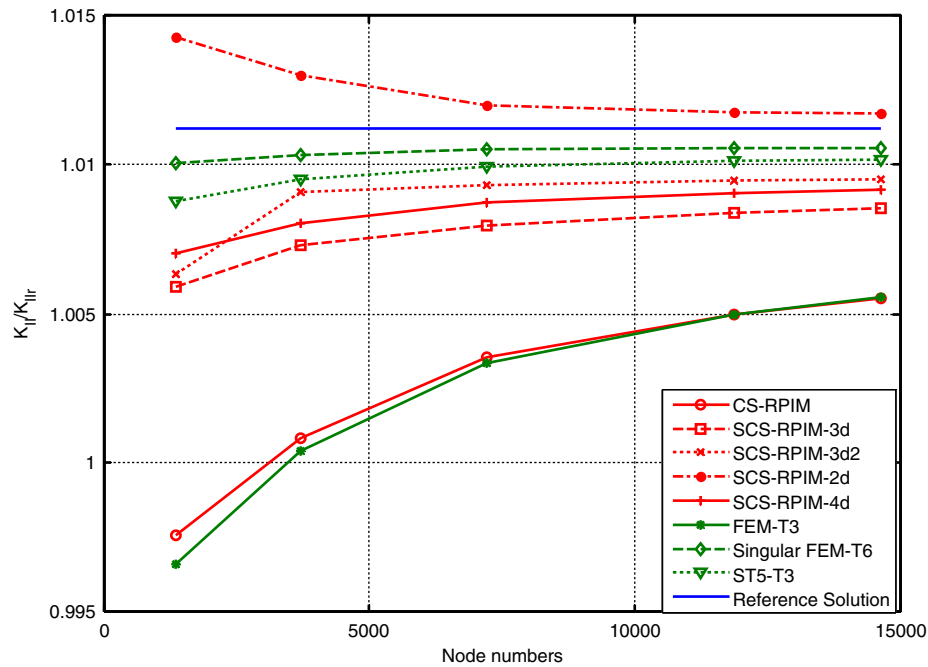


Fig. 17. An 45° inclined crack in rectangular plate under tension: the variation of normalized  $K_{II}$  with different node numbers by different methods.

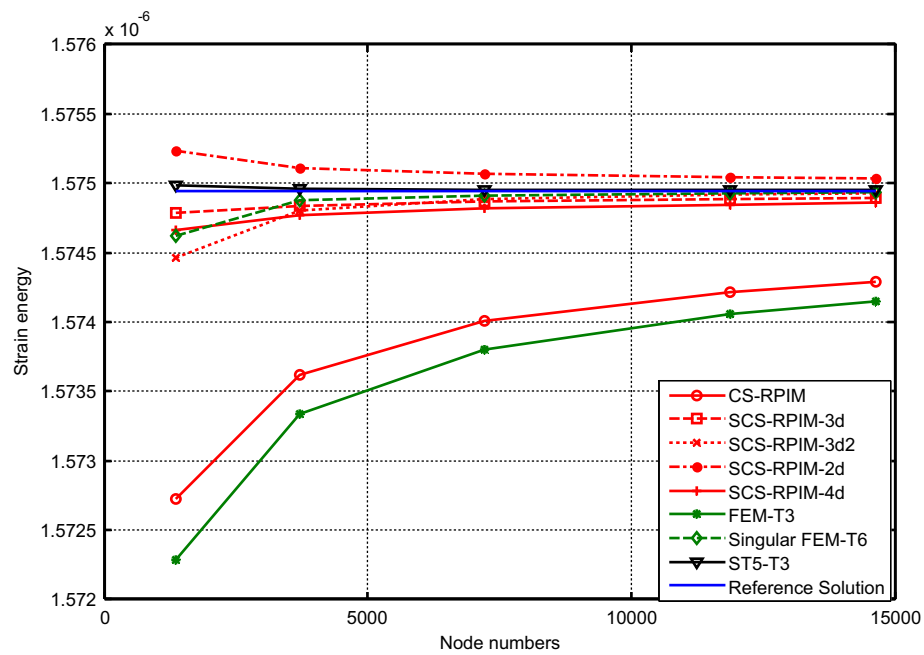


Fig. 18. An 60° inclined crack in rectangular plate under tension: the variation of strain energy with different node numbers by different methods.

The reference solutions of strain energy and SIFs are obtained using the singular FEM-T6 with a very fine mesh (401,677 nodes). The computed SIFs,  $K_I$  and  $K_{II}$ , are normalized by the reference solutions  $K_{Ir}$  and  $K_{IIr}$ , respectively.

The strain energy and the normalized SIFs for this example obtained using different numerical methods are plotted and listed in Figs. 10–12 and Tables 7–9. It can be seen again that the strain energy and the SIFs obtained by different schemes of SCS-RPIM approach the exact solutions much better than those of the standard FEM-T3 with the same mesh. The singular element devised in this work proves to be effective again. The strain energy obtained by SCS-RPIM-2d and that by singular FEM-T6 are listed

and compared in Table 10. Also the error of the strain energy to the reference solution is listed. From the table we can see that SCS-RPIM-2d has a more accurate strain energy compared to singular FEM-T6 with the same number of nodes.

### 5.3. An inclined crack in rectangular plate under tension

Each of the specimens in the previous two examples only contains one crack tip. To demonstrate the wide applicability of our method, an inclined crack with two crack tips in rectangular plate under tension is considered in this example, shown in Fig. 13. The plate is 10 mm × 10 mm, with a  $\theta$  inclined crack from the horizon-

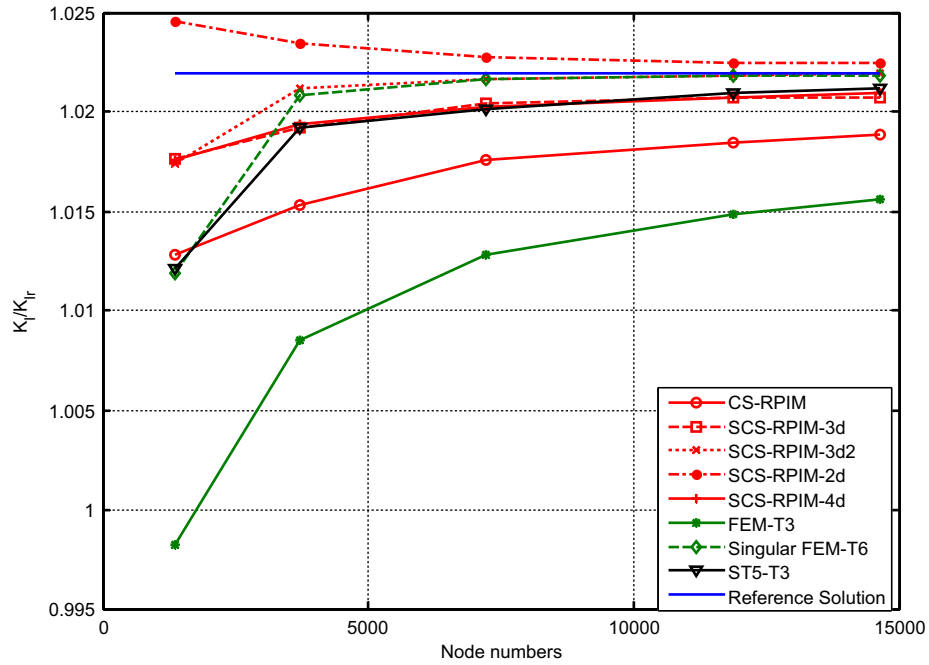


Fig. 19. An 60° inclined crack in rectangular plate under tension: the variation of normalized  $K_I$  with different node numbers by different methods.

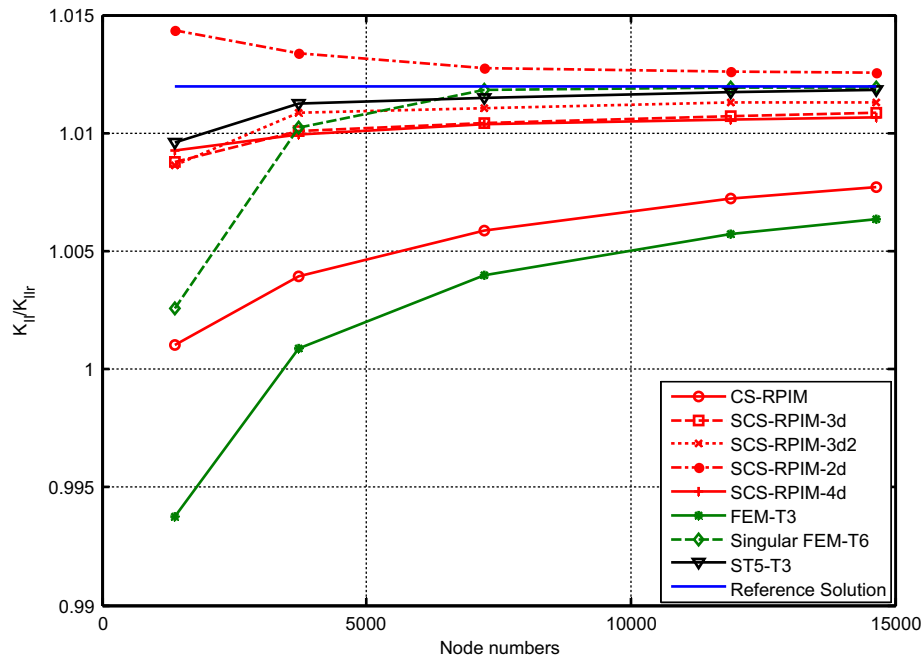


Fig. 20. An 60° inclined crack in rectangular plate under tension: the variation of normalized  $K_{II}$  with different node numbers by different methods.

**Table 11**  
Plate with an 45° inclined crack under tension: strain energy with different meshes and different schemes ( $\times 10^{-6}$ ) (reference solution is  $1.5874 \times 10^{-6}$ ).

Mesh	37 × 37	61 × 61	85 × 85	109 × 109	121 × 121
CS-RPIM	1.5832	1.5850	1.5857	1.5861	1.5862
SCs-RPIM-3d	1.5869	1.5871	1.5872	1.5873	1.5873
SCS-RPIM-3d2	1.5871	1.5874	1.5874	1.5874	1.5874
SCS-RPIM-2d	1.5876	1.5876	1.5875	1.5875	1.5875
SCS-RPIM-4d	1.5868	1.5870	1.5871	1.5872	1.5872
FEM-T3	1.5821	1.5842	1.5851	1.5856	1.5858
Singular FEM-T6	1.5870	1.5873	1.5874	1.5874	1.5874
ST5-T3	1.5869	1.5871	1.5872	1.5873	1.5873

**Table 12**  
Plate with an 45° inclined crack under tension: normalized  $K_I$  with different meshes and different schemes (reference solution is 1.0216).

Mesh	37 × 37	61 × 61	85 × 85	109 × 109	121 × 121
CS-RPIM	1.0095	1.0123	1.0145	1.0159	1.0163
SCS-RPIM-3d	1.0190	1.0195	1.0198	1.0201	1.0202
SCS-RPIM-3d2	1.0172	1.0181	1.0188	1.0192	1.0193
SCS-RPIM-2d	1.0187	1.0192	1.0196	1.0197	1.0198
SCS-RPIM-4d	1.0163	1.0173	1.0182	1.0187	1.0189
FEM-T3	0.9968	1.0076	1.0135	1.0140	1.0142
Singular FEM-T6	1.0181	1.0193	1.0201	1.0203	1.0203
ST5-T3	1.0122	1.0158	1.0173	1.0181	1.0183

**Table 13**  
Plate with an 45° inclined crack under tension: normalized  $K_{II}$  with different meshes and different schemes (reference solution is 1.0112).

Mesh	37 × 37	61 × 61	85 × 85	109 × 109	121 × 121
CS-RPIM	0.9976	1.0009	1.0035	1.0050	1.0055
SCS-RPIM-3d	1.0059	1.0073	1.0080	1.0084	1.0085
SCS-RPIM-3d2	1.0064	1.0091	1.0093	1.0099	1.0095
SCS-RPIM-2d	1.0143	1.0130	1.0120	1.0118	1.0117
SCS-RPIM-4d	1.0071	1.0080	1.0087	1.0091	1.0092
FEM-T3	0.9966	1.0033	1.0043	1.0050	1.0056
Singular FEM-T6	1.0100	1.0103	1.0105	1.0106	1.0106
ST5-T3	1.0088	1.0095	1.0099	1.0101	1.0102

**Table 14**  
The comparison of strain energy ( $\times 10^{-6}$ ) and error for plate with a 45° inclined crack under tension by between SCS-RPIM-3d2 and singular FEM-T6.

Node number	SCS-RPIM-3d2 (error %)	Singular FEM-T6 (error %)
1369	1.58709 (0.027)	1.5869076 (0.0342)
3721	1.58735 (0.00630)	1.5873046 (0.00916)
7225	1.58740 (0.00315)	1.5873678 (0.00518)
11,881	1.58742 (0.00189)	1.5873928 (0.00360)
14,641	1.58743 (0.00126)	1.5874062 (0.00276)

**Table 15**  
Plate with an 60° inclined crack under tension: strain energy with different meshes and different schemes ( $\times 10^{-6}$ ) (reference solution is  $1.574942 \times 10^{-6}$ ).

Mesh	37 × 37	61 × 61	85 × 85	109 × 109	121 × 121
CS-RPIM	1.57272	1.57362	1.57400	1.57422	1.57429
SCS-RPIM-3d	1.57478	1.57483	1.57486	1.57488	1.57489
SCS-RPIM-3d2	1.57446	1.57480	1.57488	1.57492	1.57493
SCS-RPIM-2d	1.57523	1.57511	1.57506	1.57504	1.57503
SCS-RPIM-4d	1.57466	1.57476	1.57481	1.57484	1.57486
FEM-T3	1.57228	1.57334	1.57380	1.57405	1.57414
Singular FEM-T6	1.57462	1.57487	1.57491	1.57493	1.57494
ST5-T3	1.574982	1.574957	1.574955	1.574955	1.574955

**Table 16**  
Plate with an 60° inclined crack under tension: normalized  $K_I$  with different meshes and different schemes (reference solution is 1.0219).

Mesh	37 × 37	61 × 61	85 × 85	109 × 109	121 × 121
CS-RPIM	1.0128	1.0153	1.0176	1.0185	1.0189
SCS-RPIM-3d	1.0176	1.0192	1.0204	1.0207	1.0207
SCS-RPIM-3d2	1.0174	1.0212	1.0217	1.0218	1.0219
SCS-RPIM-2d	1.0246	1.0235	1.0228	1.0225	1.0225
SCS-RPIM-4d	1.0176	1.0194	1.0203	1.0207	1.0210
FEM-T3	0.9982	1.0085	1.0128	1.0148	1.0156
Singular FEM-T6	1.0119	1.0208	1.0217	1.0218	1.0218
ST5-T3	1.0121	1.0192	1.0202	1.0209	1.0212

**Table 17**  
Plate with an 60° inclined crack under tension: normalized  $K_{II}$  with different meshes and different schemes (reference solution is 1.0120).

Mesh	37 × 37	61 × 61	85 × 85	109 × 109	121 × 121
CS-RPIM	1.0010	1.0039	1.0059	1.0072	1.0077
SCS-RPIM-3d	1.0088	1.0101	1.0105	1.0107	1.0109
SCS-RPIM-3d2	1.0086	1.0109	1.0111	1.0113	1.0113
SCS-RPIM-2d	1.0144	1.0134	1.0128	1.0126	1.0126
SCS-RPIM-4d	1.0093	1.0100	1.0104	1.0106	1.0107
FEM-T3	0.9938	1.0009	1.0040	1.0056	1.0064
Singular FEM-T6	1.0026	1.0102	1.0118	1.0119	1.0119
ST5-T3	1.0096	1.0112	1.0115	1.0117	1.0118

tal line in the center of the plate. The crack length is  $2a = \sqrt{2}$  mm. In this simulation, two values of  $\theta$ , 45° and 60° will be used. The Young's modulus of the plate is  $E = 30$  MPa and the Poisson's ratio

**Table 18**  
The comparison of strain energy ( $\times 10^{-6}$ ) and error for plate with an 60° inclined crack under tension by between SCS-RPIM-3d2 and singular FEM-T6.

Node number	SCS-RPIM-3d2 (error %)	Singular FEM-T6 (error %)
1369	1.57446 (0.0306)	1.5869076 (0.0204)
3721	1.57480 (0.00902)	1.5873046 (0.00457)
7225	1.57488 (0.00394)	1.5873678 (0.00203)
11,881	1.57492 (0.00140)	1.5873928 (0.000762)
14,641	1.57493 (0.000763)	1.5874062 (0.000127)

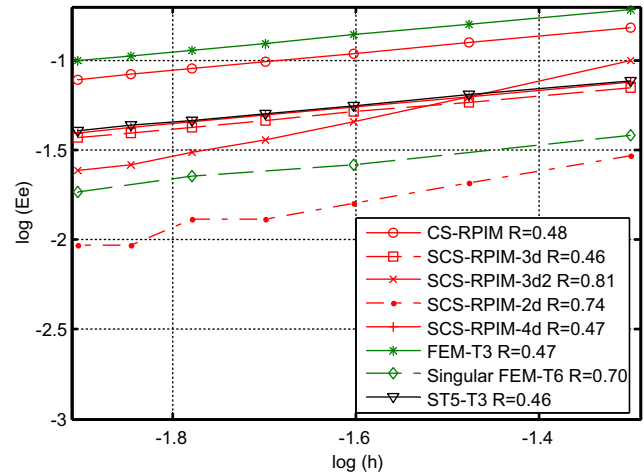


**Fig. 21.** Convergence rate of different methods for the plate with edge crack under remote tension.

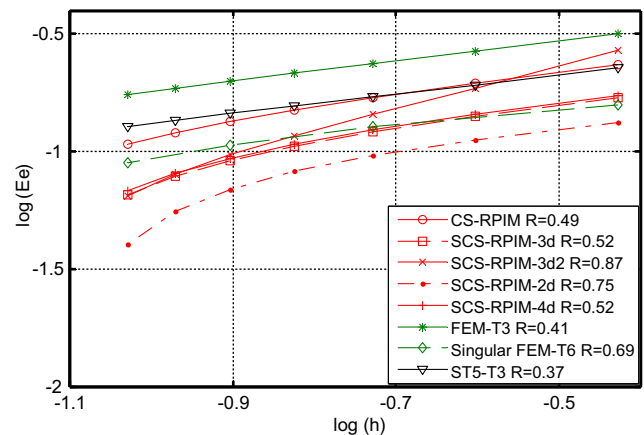


**Fig. 22.** Convergence rate of different methods for the plate with edge crack under shear.

$\nu = 0.3$ . The tension load  $\sigma = 1$  Pa is applied on the top edge. The plate is assumed to be under plane strain condition.

We discretize the model with different mesh densities ( $37 \times 37$ ,  $61 \times 61$ ,  $85 \times 85$ ,  $109 \times 109$  and  $121 \times 121$ ). The mesh of the model is shown in Fig. 14. The reference solution of strain energy and SIFs are calculated by singular FEM with 766,305 and 578,582 nodes for  $\theta = 45^\circ$ ,  $60^\circ$ , respectively. The results are plotted in Figs. 15–20 and listed in Tables 11–13 and 15–17. Note that the computed  $K_I$ ,  $K_{II}$  are normalized by  $K_{Ir}$ ,  $K_{Iir}$  given by Eq. (44)

$$\begin{aligned} K_{Ir} &= K_{I0} \cos^2 \theta \\ K_{Iir} &= K_{I0} \cos \theta \sin \theta \end{aligned} \tag{44}$$

where  $K_{I0}$  is the stress intensity factor of pure Mode I crack, when  $\theta = 0^\circ$ .

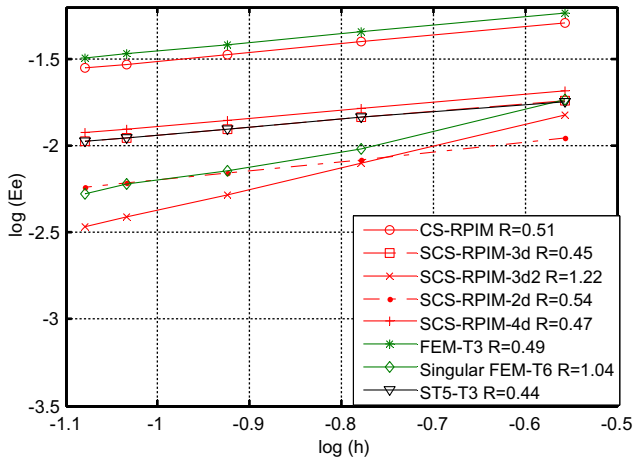


Fig. 23. Convergence rate of different methods for an 45° inclined crack in rectangular plate under tension.

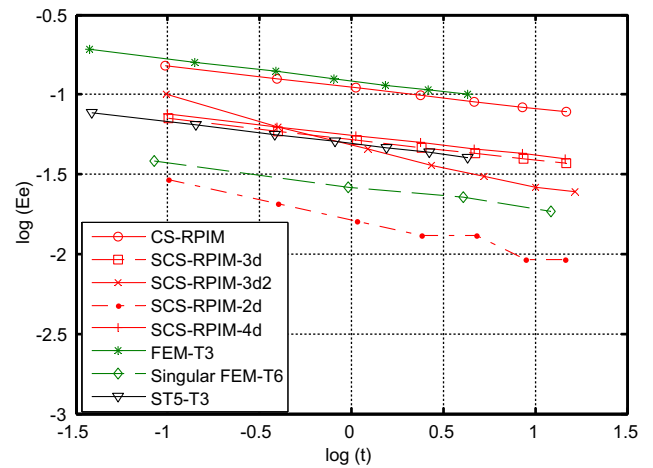


Fig. 25. Efficiency of different methods for the plate with edge crack under remote tension.

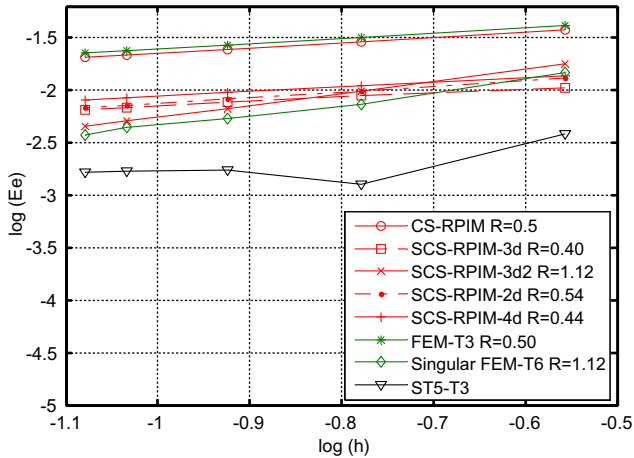


Fig. 24. Convergence rate of different methods for an 60° inclined crack in rectangular plate under tension.

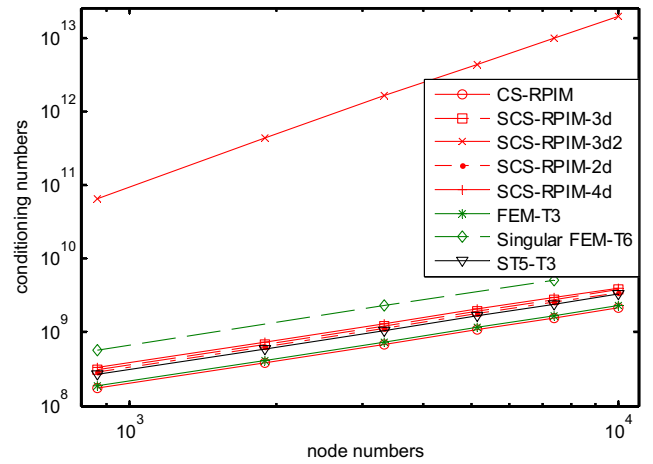


Fig. 26. Condition numbers of different methods for the plate with edge crack under remote tension.

$$K_{10} = \sigma\sqrt{\pi a} \tag{45}$$

From the results, we can see CS-RPIM and different schemes of singular CS-RPIM provide more accurate solutions than FEM-T3. SCS-RPIM-2d provides a very tight upper bound solution and the other methods give lower bound solutions in strain energy norm.

In addition, the error of the strain energy to the reference solution is listed in Tables 14 and 18. From the tables, we can see that SCS-RPIM-3d2 has a more accurate strain energy compared with singular FEM-T6 when  $\theta = 45^\circ$ , but when  $\theta = 60^\circ$  the results are less accurate than singular FEM-T6.

5.4. Convergence rate and efficiency of SCS-RPIM

To investigate convergence and efficiency of the present methods, the first example is employed with different mesh densities. The convergence rates of different methods adopted in this work are calculated and compared. To investigate quantitatively the numerical results, the error indicator in energy norm is defined as follows:

$$E_e = \sqrt{\frac{|U_{num} - U_{ref}|}{U_{ref}}} \tag{46}$$

Table 19

Time cost of different methods for plates with an edge crack problem with different mesh densities (the time cost is the average value of ten times calculation).

Mesh	21 × 41	31 × 61	41 × 81	51 × 101	61 × 121	71 × 141	81 × 161
CS-RPIM	0.09741	0.39404	1.06010	2.37530	4.63882	8.50523	14.7457
SCS-RPIM-3d	0.10116	0.39899	1.07329	2.39860	4.71257	8.67087	14.6700
SCS-RPIM-3d2	0.09837	0.39795	1.22076	2.72114	5.24141	9.98416	16.4369
SCS-RPIM-2d	0.10104	0.39939	1.07254	2.40030	4.76836	8.84753	14.5232
SCS-RPIM-4d	0.09899	0.39428	1.06177	2.38649	4.63925	8.57171	14.5967
FEM-T3	0.03758	0.14104	0.38937	0.79852	1.52512	2.59908	4.31259
Singular FEM-T6	0.08447		0.95402		4.04367		12.1366
ST5-T3	0.03884	0.14268	0.38366	0.80944	1.54554	2.63865	4.28795

**Table 20**  
Condition number of different methods for plates with an edge crack under tension with different mesh densities ( $\times 10^5$ ).

Mesh	21 × 41	31 × 61	41 × 81	51 × 101	61 × 121	71 × 141
CS-RPIM	2.0375	4.5514	8.0900	12.6664	18.2907	24.9699
SCs-RPIM-3d	3.6481	8.0913	14.3379	22.4105	32.3269	44.1000
SCS-RPIM-3d2	760.41	5147.4	19066.6	51664.4	115533	226830
SCS-RPIM-2d	3.3651	7.4520	13.1953	20.6154	29.7288	40.5475
SCS-RPIM-4d	3.8887	8.6264	15.2873	23.8955	34.4700	47.0246
FEM-T3	2.1457	4.8372	8.6338	13.5506	19.5984	26.7857
Singular FEM-T6	6.7329		26.5391		59.8711	
ST5-T3	3.1140	6.9451	12.3352	19.3046	27.8696	38.0417

**Table 21**  
The results of area integration, path integration and Gauss quadrature.

Shape function	Area integration		Path integration		Gauss quadrature	
	$\frac{\partial N}{\partial x}$	$\frac{\partial N}{\partial y}$	$Nn_x$	$Nn_y$	$Nn_x$	$Nn_y$
$N_1$	-0.0625 <i>l</i>	-0.0625 <i>l</i>	-0.0625 <i>l</i>	-0.0625 <i>l</i>	-0.0621 <i>l</i>	-0.0621 <i>l</i>
$N_2$	0	0.0208 <i>l</i>	0	0.0208 <i>l</i>	0	0.0210 <i>l</i>
$N_3$	0.0208 <i>l</i>	0	0.0208 <i>l</i>	0	0.0210 <i>l</i>	0
$N_4$	0.1250 <i>l</i>	-0.0833 <i>l</i>	0.1250 <i>l</i>	-0.0833 <i>l</i>	0.1250 <i>l</i>	-0.0839 <i>l</i>
$N_5$	-0.0833 <i>l</i>	0.1250 <i>l</i>	-0.0833 <i>l</i>	0.1250 <i>l</i>	-0.0839 <i>l</i>	0.1250 <i>l</i>

where  $U_{ref}$  denotes the strain energy of reference solution and  $U_{num}$  stands for the strain energy of numerical solution. The errors in strain energy norm against  $h$  for four different models are plotted in Figs. 21–24.  $h$  is the average distance between two adjacent nodes. From these figures, it can be seen that SCS-RPIM-3d2 has the highest convergence rate among the methods adopted in this paper in all these four models. SCS-RPIM-2d has an excellent accuracy in energy norm in most of these four models. In the third and fourth models, we use uneven meshes with more nodes near the crack tip shown in Fig. 14. However, the dimension  $h$  is obtained by the average distance of two adjacent nodes. So in these two models, we can have convergence rate even higher than 1.

The efficiency of different methods for the plate with edge crack under remote tension is plotted in Fig. 25. From the figure, it can be seen that SCS-RPIM-2d has the highest efficiency. The time cost for each method is listed in Table 19, which is the average value of ten times calculations on computer.

The condition number of the global stiffness matrix,  $cond(K)$ , is an important indicator for the numerical property of a numerical method. When an iteration solver is used to solve the algebraic system equation, it affects directly the number of iterations needed to obtain a converged solution in the manner of  $n_{iter} \propto \sqrt{cond(K)}$ . The condition number of different methods for the first example against node numbers is plotted in Fig. 26 and listed in Table 20. As it can be seen, CS-RPIM has the smallest condition number among all the methods in this work with the same mesh. SCS-RPIM-3d, SCS-RPIM-2d and SCS-RPIM-4d perform better than singular FEM-T6 in condition number. However, SCS-RPIM-3d2 doesn't perform well as it does in convergence rate and efficiency.

**6. Conclusion**

In this work, a cell-based smoothed radial point interpolation method (CS-RPIM) is developed and applied to the fracture problems. A five-node element is used to simulate the singular behavior of stress and strain in the vicinity of the crack tip. Several different schemes of SCS-RPIM are devised for strain smoothing operation over the five-node element. The present methods are used to solve some fracture problems and the results are compared with those of FEM-T3 and singular FEM-T6. The comparison has demonstrated the effectiveness of the proposed methods. Some conclusions can be drawn as follows:

1. The number of the Gauss points affects the accuracy of the computing, in this work the number of the Gauss points is set to 4. Also, the domain independence of stress intensity factors (SIFs) is observed.
2. CS-RPIM can have more accurate results than FEM-T3 with the same mesh. Among the different singular schemes, SCS-RPIM-2d generally provides very tight upper bound for strain energy and SIFs. Other schemes generally give much tighter lower bound solutions compared to the FEM-T3.
3. Among all the methods adopted in this paper, SCS-RPIM-3d2 has the highest convergence rate, SCS-RPIM-2d has the highest efficiency, and CS-RPIM has the smallest condition number.

**Appendix.**

Owing to the  $1/\sqrt{r}$  singular strain in the crack tip, there is still doubt whether it is feasible to apply the divergence theorem to the area integration. In order to testify our results are accurate, in this appendix we would like to compare the results of the path integration with the exact results of the area integration.

We use an isosceles rectangular singular element with the dimension shown in Fig. 27. The shape functions along the edge are as follows:

$$N_1 = 1 + 2\frac{r}{l} - 3\sqrt{\frac{r}{l}}, \quad N_2 = 2\frac{r}{l} - \sqrt{\frac{r}{l}}, \quad N_4 = -4\frac{r}{l} + 4\sqrt{\frac{r}{l}} \quad (47)$$

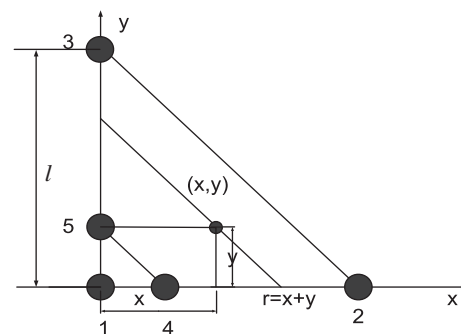


**Fig. 27.** Isosceles rectangular singular element around the crack tip.

Here  $r$  is the distance between the point and the crack tip.  $l$  is the length of the edge originating from the crack tip.

The shape functions of the points inside the triangular element are as follows:

$$\begin{aligned} N_1 &= 1 + 2\frac{x+y}{l} - 3\sqrt{\frac{x+y}{l}} \\ N_2 &= \left(2\frac{x+y}{l} - \sqrt{\frac{x+y}{l}}\right) * \frac{x}{x+y} \\ N_3 &= \left(2\frac{x+y}{l} - \sqrt{\frac{x+y}{l}}\right) * \frac{y}{x+y} \\ N_4 &= \left(-4\frac{x+y}{l} + 4\sqrt{\frac{x+y}{l}}\right) * \frac{x}{x+y} \\ N_5 &= \left(-4\frac{x+y}{l} + 4\sqrt{\frac{x+y}{l}}\right) * \frac{y}{x+y} \end{aligned} \quad (48)$$

Here  $(x, y)$  is the coordinate of the point inside the element. Then the derivatives of the shape functions with respect to  $x, y$  are listed as follows:

$$\begin{aligned} \frac{\partial N_1}{\partial x} &= \frac{2}{l} - 3\frac{1}{2\sqrt{l(x+y)}}, & \frac{\partial N_1}{\partial y} &= \frac{2}{l} - 3\frac{1}{2\sqrt{l(x+y)}} \\ \frac{\partial N_2}{\partial x} &= \frac{2}{l} - \frac{2l(x+y) - xl}{2(l(x+y))^{3/2}}, & \frac{\partial N_2}{\partial y} &= \frac{1}{2} \frac{x}{\sqrt{l}} (x+y)^{-3/2} \\ \frac{\partial N_3}{\partial x} &= \frac{1}{2} \frac{y}{\sqrt{l}} (x+y)^{-3/2}, & \frac{\partial N_3}{\partial y} &= \frac{2}{l} - \frac{2l(x+y) - yl}{2(l(x+y))^{3/2}} \\ \frac{\partial N_4}{\partial x} &= \frac{-4}{l} + 4\frac{2l(x+y) - xl}{2(l(x+y))^{3/2}}, & \frac{\partial N_4}{\partial y} &= -2(x+y)^{-3/2} \frac{x}{\sqrt{l}} \\ \frac{\partial N_5}{\partial x} &= -2(x+y)^{-3/2} \frac{y}{\sqrt{l}}, & \frac{\partial N_5}{\partial y} &= \frac{-4}{l} + 4\frac{2l(x+y) - yl}{2(l(x+y))^{3/2}} \end{aligned} \quad (49)$$

We integrate the derivatives over the triangular domain 1-4-5, because the singularity only exists in 1-4-5 triangular domain. The results are listed in the following table. Also the integration of the shape functions along the boundary is calculated and compared. The results of four Gauss quadrature points are also listed in Table 21 and compared. From Table 21, it can be seen that the integration of the singular derivatives of the shape functions over the triangular domain are exactly the same with the results of the path integration of the shape functions multiplied by the unit outward vector component along the boundary of the triangular domain. That is to say that Divergence theorem is applicable for the singular shape functions. The results of Gauss quadrature are very close to the exact values.

## References

- [1] Zienkiewicz OC, Taylor RL. The finite element method. fifth ed. Oxford, UK: Butterworth Heinemann; 2000.
- [2] Liu GR, Quek SS. The finite element method: a practical course. Oxford: Butterworth Heinemann; 2003.
- [3] Brenner SC, Scott LR. The mathematical theory of finite element methods. Springer-Verlag; 1994.
- [4] Dietrich B. Finite elements: theory, fast solvers, and applications in solid mechanics. Cambridge University Press; 2007.
- [5] Samarskii AA, Vabishchevich PN, Vulkov LG. Finite difference methods: theory and applications. New York: Nova Science Publishers; 1999.
- [6] Forsythe GE, Wasow WR. Finite-difference methods for partial differential equations. New York: Cambridge University Press, Wiley; 1960.
- [7] Leveque RJ. Finite volume methods for hyperbolic problems. New York: Cambridge University Press; 2002.
- [8] Li RH, Chen ZY, Wu W. Generalized difference methods for differential equations: numerical analysis of finite volume methods. New York: Marcel Dekker; 2000.
- [9] Belytschko T, Black T. Elastic crack growth in finite elements with minimal remeshing. Int J Numer Methods Eng 1999;45(5):601–20.
- [10] Moës N, Dolbow J, Belytschko T. A finite element method for crack growth without remeshing. Int J Numer Methods Eng 1999;46(1):131–50.
- [11] Bordas S, Rabczuk T, Hung NX, Nguyen VP, Natarajan S, Bog T, et al [Strain smoothing in FEM and XFEM]. Comput Struct 2010;88. doi:10.1016/j.compstruc.2008.07.006 [Chapter 23–24 1419–1443].
- [12] Menk A, Bordas S. Numerically determined enrichment functions for the extended finite element method and applications to bi-material anisotropic fracture and polycrystals. Int J Numer Methods Eng 2010;83: 805–28.
- [13] Belytschko T, Gracie R, Ventura G [A review of extended/generalized finite element methods for material modeling]. Model Simul Mater Sci Eng 2009. doi:10.1088/0965-0393/17/4/043001.
- [14] Chessa J, Wang Hw, Belytschko T. On the construction of blending elements for local partition of unity enriched finite elements. Int J Numer Methods Eng 2003;57:1015–38.
- [15] Xiao QZ, Karihaloo BL. Improving the accuracy of XFEM crack tip fields using higher order quadrature and statically admissible stress recovery. Int J Numer Methods Eng 2006;66(9):1378–410.
- [16] Rabczuk T, Bordas S, Zi G. On three-dimensional of crack growth using partition of unity methods. Comput Struct 2010;88:1391–411.
- [17] Rabczuk T, Bordas S, Zi G. A three-dimensional meshfree method for continuous multiple-crack initiation, propagation and junction in statics and dynamics. Comput Mech 2007;40(3):473–95. ISBN/ISSN: 0178-7675, doi:10.1007/s00466-006-0122-1.
- [18] Wyart E, Coulon D, Duflo M, Pardoën T, Remacle JF, Lani F. A substructured FE-shell/XFE-3D method for crack analysis in thin-walled structures. Int J Numer Methods Eng 2007;72:757–79.
- [19] Bordas SPA, Conley JG, Moran B, Gray J, Nichols E. A simulation-based design paradigm for complex cast components. Eng Comput 2007;23(1): 25–37.
- [20] Bordas S, Moran B. Enriched finite elements and level sets for damage tolerance assessment of complex structures. Eng Fract Mech 2006;73(9):1176–201.
- [21] Karihaloo BL, Xiao QZ. Accurate determination of the coefficients of elastic crack tip asymptotic field by a hybrid crack element with p-adaptivity. Eng Fract Mech 2001;68:1609–30.
- [22] Xiao QZ, Karihaloo BL. An overview of a hybrid crack element and determination of its complete displacement field. Eng Fract Mech 2007;74:1107–17.
- [23] Liu GR. A generalized gradient smoothing technique and the smoothed bilinear form for Galerkin formulation of a wide class of computational methods. Int J Comput Methods 2008;5:199–236.
- [24] Xuan ZC, Lassila T, Rozza G, Quarteroni A. On computing upper and lower bounds on the outputs of linear elasticity problems approximated by the smoothed finite element method. Int J Numer Methods Eng; 2010. doi:10.1002/nme.2825.
- [25] Nguyen-Xuan H, Bordas S, Nguyen-Dang H. Smooth finite element methods: convergence, accuracy and properties. Int J Numer Methods Eng 2008;74(2):175–208.
- [26] Vinh Phu Nguyen, Rabczuk T, Bordas S, Duflo M. Meshless methods: A review and computer implementation aspects. Mathematics and Computers in Simulation 2008;79:763–813.
- [27] Liu GR. On G space theory. Int J Comput Methods 2009;6(2):257–89.
- [28] Chen JS, Wu CT, Yoon Y. A stabilized conforming nodal integration for Galerkin mesh-free methods. Int J Numer Methods Eng 2001;50:435–66.
- [29] Liu GR, Zhang GY. A normed G space and weakened weak formulation of a cell-based smoothed point interpolation method. Int J Comput Methods 2009;6(1):147–79.
- [30] Liu GR. A G space theory and weakened weak (W<sup>2</sup>) form for a unified formulation of compatible and incompatible methods, Part I: Theory and Part II: Applications to solid mechanics problems. Int J Numer Methods Eng 2010;81(9):1093–156.
- [31] Liu GR. Meshfree methods: moving beyond the finite element method. 2nd ed. Boca Raton: Taylor & Francis/CRC Press; 2009.
- [32] Liu GR, Nguyen TT. Smoothed finite element method. Boca Raton: Taylor & Francis/CRC Press; 2010.
- [33] Liu GR, Zhang GY. Upper bound solution to elasticity problems: a unique property of the linearly conforming point interpolation method (LC-PIM). Int J Numer Methods Eng 2008;74(7):1128–61.
- [34] Liu GR, Chen L, Nguyen TT, Zeng KY, Zhang GY. A novel singular node-based smoothed finite element method (NS-FEM) for upper bound solutions of fracture problems. Int J Numer Methods Eng. doi:10.1002/nme.2868.
- [35] Liu GR. A generalized gradient smoothing technique and the smoothed bilinear form for Galerkin formulation of a wide class of computational methods. Int J Comput Methods 2008;5(2):199–236.
- [36] Nguyen-Xuan H, Liu GR. An edge-based smoothed finite element method (ES-FEM) with stabilized discrete shear gap technique for analysis of Reissner–Mindlin plates. Comput Methods Appl Mech Eng 2010;199:471–89.
- [37] Liu GR, Zhang GY, Dai KY, Wang YY, Zhong ZH, Li GY, et al. A linearly conforming point interpolation method (LC-PIM) for 2D mechanics problems. Int J Comput Methods 2005;2(4):645–65.
- [38] Zhang GY, Liu GR, Wang YY, Huang HT, Zhong ZH, Li GY, et al. A linearly conforming point interpolation method (LC-PIM) for three-dimensional elasticity problems. Int J Numer Methods Eng 2009;72:1524–43.
- [39] Chen L, Nguyen HX, Nguyen TT, Zeng KY, Wu SC. Assessment of smoothed point interpolation methods for elastic mechanics. Commun Numer Methods Eng doi:10.1002/cnm.1251.

- [40] Liu GR, Gu YT. A point interpolation method for two-dimensional solids. *Int J Numer Methods Eng* 2001;50:937–51.
- [41] Liu GR, Dai KY, Lim KM, Gu YT. A point interpolation meshfree method for static and frequency analysis of two-dimensional piezoelectric structures. *Comput Mech* 2002;29(6):510–9.
- [42] Liu GR, Gu YT. An introduction to meshfree methods and their programming. Dordrecht, the Netherlands: Springer; 2005.
- [43] Wang JG, Liu GR. A point interpolation meshless method based on radial basis functions. *Int J Numer Mech Eng* 2002;54(11):1623–48.
- [44] Wang JG, Liu GR. On the optimal shape parameters of radial basis functions used for 2-D meshless methods. *Comput Methods Appl Mech Eng* 2002;191:2611–30.
- [45] Chen L, Liu L, Nourbakhsh NN, Zeng K. A singular edge-based smoothed finite element method (ES-FEM) for biomaterial interface cracks. *Comput Mech* 2010;45:109–25.
- [46] Hardy RL. Theory and applications of the multiquadrics–biharmonic method (20 years of discovery 1968–1988). *Comput Math Appl* 1990;19:163–208.
- [47] Golberg MA, Chen CS, Bowman H. Some recent results and proposals for the use of radial basis functions in the BEM. *Eng Anal Bound Elem* 1999;23: 285–96.
- [49] Barsoum RS. On the use of isoparametric finite elements in linear fracture mechanics. *Int J Numer Methods Eng* 1976;10:551–64.
- [50] Barsoum RS. Triangular quarter-point elements as elastic and perfectly-plastic crack tip elements. *Int J Numer Methods Eng* 1977;11:85–98.